

# Hybrid Polymer Electrolyte Encased Cathode Particles Interface-Based Core–Shell Structure for High-Performance Room Temperature All-Solid-State Batteries

Sivaraj Pazhaniswamy,\* Sagar A. Joshi, Haoqing Hou, Abhilash Karuthedath Parameswaran, and Seema Agarwal\*

A smooth interfacial contact between electrode and electrolyte, alleviation of dendrite formation, low internal resistance, and preparation of thin electrolyte (<20  $\mu\text{m}$ ) are the key challenging tasks in the practical application of  $\text{Li}_7\text{La}_3\text{Zr}_2\text{O}_{12}$  (LLZO)-based solid-state batteries (SSBs). This paper develops a unique strategy to reduce interfacial resistance by designing an interface-based core–shell structure via direct integration of Al-LLZO ceramic nanofibers incorporated poly(vinylidene fluoride)/LiTFSI on the surface of a porous cathode electrode (HPEIC). This yields an ultrathin solid polymer electrolyte with a thickness of 7  $\mu\text{m}$ . The integrated HPEIC/Li SSB with  $\text{LiFePO}_4/\text{C}$  exhibits an initial specific capacity of 166  $\text{mAh g}^{-1}$  at 0.1 C and 159  $\text{mAh g}^{-1}$  with capacity retention of 100% after 120 cycles at 0.5 C (25  $^\circ\text{C}$ ). The HPEIC/Li SSB with  $\text{LiNi}_{0.8}\text{Mn}_{0.1}\text{Co}_{0.1}\text{O}_2$  cathode delivers a good discharge capacity of 134  $\text{mAh g}^{-1}$  after 120 cycles at 0.5 C. The rational design of interface-based core–shell structure outperforms the conventional assembly of solid-state cells using free-standing solid electrolytes in specific capacity, internal resistance, and rate performance. The proposed strategy is simple, cost-effective, robust, and scalable manufacturing, which is essential for the practical applicability of SSBs.

## 1. Introduction

The conventional liquid electrolyte has adverse reactions, such as a highly flammable nature and dendrite formation, which causes the battery to short-circuit, promoting the risk of fire and explosion.<sup>[1]</sup> Various catastrophes with traditional liquid-based batteries have prompted intense research focusing on entirely solid-state batteries (SSBs). The transition from flammable liquid electrolytes to solid-state electrolytes (SSEs) not only increases battery safety but also enables Li metal to be used as a superior anode material due to its unique properties of the high theoretical capacity of 3860  $\text{mAh g}^{-1}$  and low electrochemical potential  $-3.4$  V versus standard hydrogen electrode.<sup>[2,3]</sup> Thus, SSBs are predicted to be the most secure, adaptable, high-energy density, and long-lasting energy storage devices for electric vehicles and grid energy storage. The key hurdles in bringing all-SSBs to life include the rise


in the internal resistance of solid materials during cycling, poor interface compatibility, and low ionic conductivity.<sup>[4]</sup> In addition, SSEs play a vital role in optimizing the electrochemical performance of SSBs.

SSEs are broadly categorized into three types; i) solid-state inorganic electrolytes (SSIEs) which include superionic conductor  $\text{Li}_{10}\text{GeP}_2\text{S}_{12}$  (LGPS), Garnet type-  $\text{Li}_7\text{La}_3\text{Zr}_2\text{O}_{12}$  (LLZO), and perovskite  $\text{Li}_{0.5}\text{La}_{0.5}\text{TiO}_3$  (LLTO); ii) solid organic polymer electrolytes (SOPEs) (poly(ethylene oxide) (PEO), poly(vinylidene fluoride) (PVDF), polyacrylonitrile (PAN), etc., with lithium perchlorate ( $\text{LiClO}_4$ ) and lithium bis(trifluoromethane sulfonyl)imide (LiTFSI) salts); and iii) solid organic–inorganic composite electrolytes.<sup>[5]</sup> SSIEs have high ionic conductivity, a broad electrochemical stability window, and electrochemical reactivity. Nonetheless, they are primarily powders, restricting the feasibility of SSB production.<sup>[5]</sup> SOPEs offer strong flexibility, film-forming ability, and interface compatibility but have limited ionic conductivity, a narrow electrochemical stability window, low transference number, and poor mechanical stability.<sup>[6]</sup> Hence, the combination of superior properties of organic polymers with inorganic ceramic materials provides

S. Pazhaniswamy, S. A. Joshi, S. Agarwal  
Bavarian Center for Battery Technology  
Macromolecular Chemistry II  
University of Bayreuth  
95440 Bochum, Germany  
E-mail: sivaraj.pazhaniswamy@uni-bayreuth.de; agarwal@uni-bayreuth.de

H. Hou  
College of Chemistry and Chemical Engineering  
Jiangxi Normal University  
Nanchang, Jiangxi 330022, China

A. K. Parameswaran  
Department of Inorganic Chemistry  
University of Chemistry and Technology  
16628 Prague, Czech Republic

 The ORCID identification number(s) for the author(s) of this article can be found under <https://doi.org/10.1002/aenm.202202981>.

© 2022 The Authors. Advanced Energy Materials published by Wiley-VCH GmbH. This is an open access article under the terms of the Creative Commons Attribution License, which permits use, distribution and reproduction in any medium, provided the original work is properly cited.

DOI: 10.1002/aenm.202202981

an effective composite polymer electrolyte (CPE) for developing high-performance SSBs. In this regard, LLZO with cubic structure is a better solid electrolyte host due to its high ionic conductivity ( $10^{-3}$  to  $10^{-4}$  S  $\text{cm}^{-1}$  at room temperature), good electrochemical stability window ( $>5$  V), great stability against Li-metal.<sup>[2,5]</sup> However, LLZO material has poor air stability and easily generates  $\text{Li}_2\text{CO}_3$  on the surface due to subsequent contact with  $\text{CO}_2$  in air and the grain boundaries within LLZO as a result of a  $\text{Li}^+/\text{H}^+$  exchange.<sup>[5]</sup> These manifestations reduce the ionic conductivity of LLZO following air contact and drastically impair battery performance. The surface properties of LLZO can be modified by incorporating various polymer matrices such as PVDF, PEO, PAN, etc., owing to their high dielectric constant and  $\text{Li}^+$  solvating ability.<sup>[7]</sup> The PEO is the most widely explored polymer electrolyte; it has a low electrochemical stability window ( $<3.8$  V); PEO and Li salts are hygroscopic, making them unstable and have low ionic conductivity of  $10^{-6}$  S  $\text{cm}^{-1}$  at ambient temperature,<sup>[8]</sup> restricting their application in high-energy-density SSBs. The PVDF has better mechanical, thermal, and electrochemical stability than PEO.<sup>[9]</sup> The PVDF is the most often used polymer binder in fabricating electrode materials because it improves the interfacial contact between electrode and electrolytes and has superior mechanical compatibility during the charge–discharge process. Furthermore, PVDF has a strong polarization effect, dissociating lithium ions and enhancing ionic conductivity.<sup>[10]</sup> The PVDF-based polymers are a great choice for dealing with interface incompatibility difficulties in the design of hybrid solid polymer electrolytes (HPEs).

Among the numerous HPEs containing LLZO particles, the polymer/LLZO nanowires or fibers-based HPEs showed improved electrochemical window stability, ionic conductivity, flexibility, and electrochemical stability against lithium metal.<sup>[11–13]</sup> The Al substituted LLZO fiber networks were synthesized using electrospinning procedures and turned into 3D coral-like LLZO networks that were employed as free-standing 3D active nanofiller in a PVDF/ $\text{LiClO}_4$  with a thickness of 100  $\mu\text{m}$ .<sup>[14]</sup> The mechanical stability of the 3D coral-like CPE was up to 5.9 MPa, with an ionic conductivity of  $1.51 \times 10^{-4}$  S  $\text{cm}^{-1}$  and a transference number of 0.47. Yirui et al.<sup>[15]</sup> used the blow-spinning method to create a 3D LLZO nanofiber framework and made a composite with PVDF-HFP and PPC to produce a free-standing and flexible CPE (100  $\mu\text{m}$ ). Recently, Tadesu et al.<sup>[16]</sup> prepared Aluminium-doped LLZO (Al-LLZO) nanofibers embedded PVDF-based free-standing hybrid SSE (184  $\mu\text{m}$ ) and reported an initial capacity of 162 mAh  $\text{g}^{-1}$  with capacity retention of 92.41% after 100 cycles at 0.1 C. Mengmeng et al.<sup>[17]</sup> synthesized CPE by integrating 3D-LLZO fibers into PVDF-PEO hybrid polymer matrices containing LiTFSI salt. It delivered discharge capacities of 141.4, 141.5, 143.3, 139.7, and 130.8 mAh  $\text{g}^{-1}$  at different current rates of 0.2, 0.3, 0.5, 1, and 2 C. Xuewen et al.<sup>[2]</sup> fabricated free-standing PEO/LLZO nanofibers CPE (62  $\mu\text{m}$ ) by quenching in liquid nitrogen. The SSB delivered an initial discharge capacity of 138 mAh  $\text{g}^{-1}$  with capacity retention of 74.8% after 300 cycles at 0.5 C. According to the literature review, all prior investigations developed free-standing polymer/LLZO-based solid electrolytes with a high thickness (40–184  $\mu\text{m}$ ) that exhibit poor interface contact and high interfacial resistance. Very few SSBs

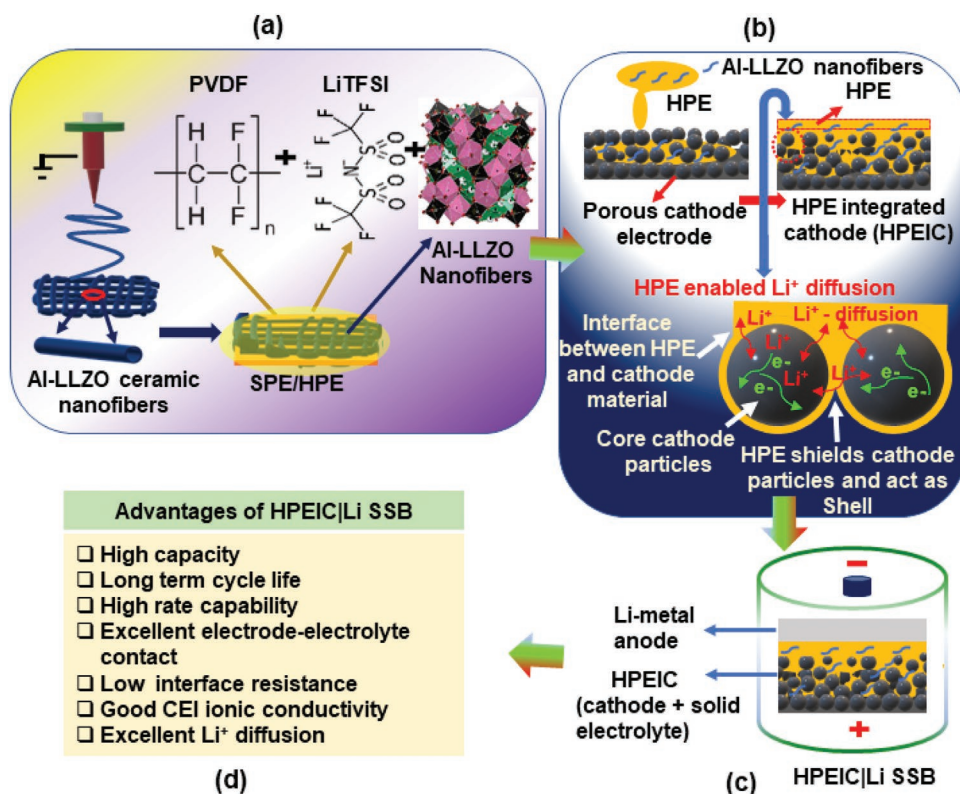
demonstrate reasonable electrochemical performance due to their high electrode/electrolyte interface resistance, poor interface compatibility between cathode and electrolytes, and high operating temperature (40–70 °C).<sup>[5,18–21]</sup> The LLZO-based SSBs suffer from lithium dendrite formation during battery operation when lithium metal is used as an anode.<sup>[5]</sup> Numerous studies revealed mechanical, thermal, and ionic conductivity improvements but failed to suppress dendrite formation at high current densities, minimize the thickness, and improve solid–solid interface contact.<sup>[5,14–17]</sup> The inhomogeneous contact of LLZO particles with the lithium anode results in high interface resistance and lithium dendrites. Hence, the design of a smooth interfacial contact between electrode and electrolyte, reducing the dendrite growth, decreasing interface resistance, porosity of the cathode electrode, preparing thin electrolyte ( $<20$   $\mu\text{m}$ ), and improving the interfacial contact are the major challenges in the practical application of LLZO-based SSBs.

These significant challenges were addressed in this work by employing a unique strategy. We prepared a very thin solid electrolyte ( $\approx 7$   $\mu\text{m}$ ), by designing an interface-based core–shell structure with direct integration of PVDF/LiTFSI/Al-LLZO hybrid polymer electrolyte (HPE) on the surface of a porous LFP and NMC811 cathode electrodes (**Scheme 1a–d**) which is the first report on developing a very thin electrolyte among the reported LLZO-based SSB scenarios. The optimized composition of Al-doped LLZO ceramic nanofibers in HPE is infused into the surface of the cathode using a three-step process that fills the pores and micro-voids of the electrode, reducing pore inadequacies and improving adhesion between the cathode and electrolyte interface as shown in **Scheme 1b**. In this process, the composite polymer uniformly covered the cathode particles, preventing cathode particle cracking during the charge–discharge process. The low viscous HPE solution with carbon additive coated on the porous cathode significantly improved Li-ion diffusion in the cathode and solid electrolytes. This method makes it easier to produce a thin solid electrolyte, dramatically reduces interfacial resistance, and improves the electrochemical performance of cathode materials. The integrated LFP-HPEIC/Li SSB delivered a high capacity of 159 mAh  $\text{g}^{-1}$  with capacity retention of 100% after 120 cycles at 0.5 C rate at 25 °C. The interface-based core–shell structured HPEIC exhibits lower internal resistance and high Li-ion diffusion, good specific capacity, and rate performance.

## 2. Results and Discussion

### 2.1. Material Characterizations

Al-LLZO ceramic nanofibers with the cubic structure were prepared using electrospinning of a precursor solution with polyvinylpyrrolidone (PVP) template polymer followed by the calcination of the as-spun nanofibers. The thermogravimetric analysis (TGA) was carried out to optimize the calcination temperature of Al-LLZO nanofibers, as shown in **Figure 1a**. As spun Al-LLZO nanofibers exhibit different weight losses, with a 14% weight loss due to solvent evaporation and a significant weight loss (30%) recorded at temperatures ranging from 300 to 400 °C due to PVP polymer matrix degradation. A weight loss



**Scheme 1.** Schematic representation: a) Fabrication of HPEs, b) design of interface-based core-shell and HPE enabled Li-ion diffusion, c) integrated HPEIC|Li SSB, and d) advantages of HPEIC over free-standing solid electrolytes.

started at 500 °C and ended at 700 °C as a result of the parent chemical processes of the LLZO precursors. There is no weight loss after 700 °C, confirming the formation of Al-LLZO crystal structure.<sup>[22]</sup> Consequently, the calcination temperature was fixed between 600 and 800 °C to obtain pure phase Al-LLZO nanofibers. The X-ray diffraction (XRD) pattern of Al-LLZO ceramic nanofibers calcined at 600, 700, and 800 °C for 3 h at a heating rate of 1° min<sup>-1</sup> is shown in Figure S1a–c, Supporting Information. The impurity phase La<sub>2</sub>O<sub>3</sub> (Joint Committee on Powder Diffraction Standards card: 96-200-2287) is observed in Al-LLZO nanofibers calcined at 600 and 700 °C (indicated as ♦ in Figure S1a,b, Supporting Information). The impurity peaks in Al-LLZO at 700 °C are less visible than in the sample calcined at 600 °C (Figure S1b, Supporting Information). The Al-LLZO nanofibers calcined at 800 °C show a cubic structure (space group Ia3d) with no impurity phases (Figure S1c, Supporting Information), which is consistent with previous studies<sup>[22,23]</sup> and ICDD data (96-155-2154).

Furthermore, the XRD patterns of the samples are computationally fitted using Rietveld refinement (Fullprof software) to enumerate the impurity phase (La<sub>2</sub>O<sub>3</sub>) and Al-LLZO phase and acquire the accurate cubic lattice parameters, as shown in Figure 1b–d. The refinement results are listed in Table S1, Supporting Information. The refinement results (Table S1, Supporting Information) imply that the cubic lattice cell parameter of Al-LLZO at 800 °C is 12.986 Å, which is comparable to the value ( $a = 12.972$  Å) reported by Mengesha et al.<sup>[16]</sup> The findings demonstrate that La, Zr, and O ions occupied the 24c, 16a, and 96h sites in the cubic phase of Al-LLZO nanofibers, while

Li<sub>1</sub> and Li<sub>2</sub> ions occupied the 24d and 96h sites (Figure S2 and Table S1, Supporting Information). The refinement of the XRD pattern ensured that the Al<sup>3+</sup> ions could be occupied at the 24d position, which is a necessary arrangement for interconnecting the Li<sup>+</sup> ion diffusion in the Al-LLZO nanofiber.<sup>[24]</sup> The preparation of electrochemically stable cubic structure LLZO is the key problem at the material level. It could be obtained via solid-state or other chemical processes at high-temperature calcination at roughly 1100 °C. However, the high-temperature calcination produces large particle sizes (5–7 μm), resulting in high grain and grain boundary resistance. These microparticles are difficult to disperse uniformly in the polymer host and high grain boundary resistance has an impact on electrochemical performance. As a result, Al-LLZO ceramic nanofibers with a cubic structure were prepared in this study by electrospinning a precursor solution containing PVP template polymer and optimized the calcination temperature of the as-spun nanofibers.

Ceramic nanowires have been investigated as electrode materials for electrochemical energy storage devices. The electrospinning technology has been approved as a method of producing polymer, composite, ceramic, and carbon nanofibers. Ceramic nanofibers are normally made by electrospinning ceramic precursors in the presence of polymer, followed by calcination at higher temperatures. The high-quality short ceramic nanofibers were prepared by optimizing the parameters such as optimum polymer and a sol-gel precursor, electrospinning of the solution under appropriate conditions to generate nanofibers containing inorganic precursor and calcination of the as-spun nanofibers at appropriate temperature to remove

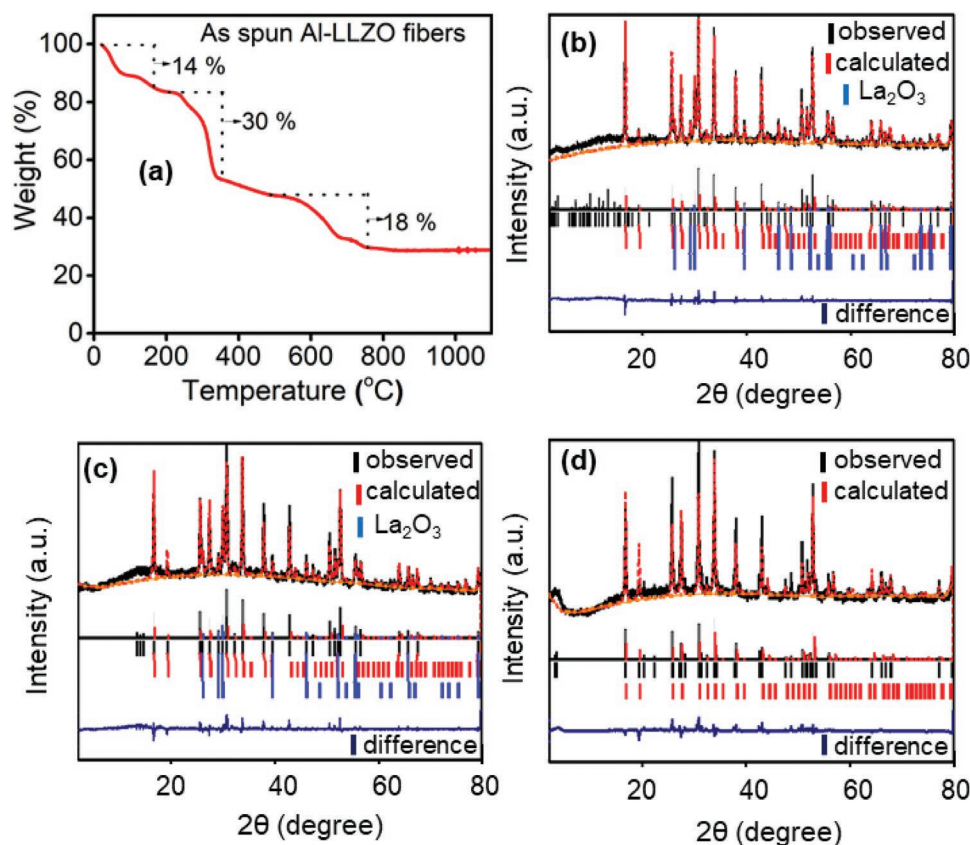


**Figure 1.** a) TGA curve of as spun Al-LLZO ceramic nanofibers; Rietveld refined XRD patterns of Al-LLZO nanofibers: b) calcined at 600 °C, c) calcined at 700 °C, and d) calcined at 800 °C.

polymers.<sup>[25]</sup> In this work, the concentration of PVP has been tuned by altering the different wt% of PVP polymer (Figure S3, Supporting Information). The polymer solution concentration influences the formation of ceramic nanofibers and their size, diameter, and final product. Low polymer concentration electrospinning produces a variety of beads and non-uniform fiber diameters. The low concentration of PVP loading into the electrospinning syringe caused a surface tension and electrical force effect during liquid jet formation at the tip of the needle, resulting in the development of beads on nanofiber surfaces. The quantity of polymer decomposition during calcination was more noticeable at high PVP polymer concentrations, resulting in non-fibrous Al-LLZO powder and less Al-LLZO content. Among the various PVP concentrations tested, the Al-LLZO precursor solution containing 10 wt% PVP produced more uniform and short ceramic nanofibers; hence 10% was chosen as the optimal concentration for producing Al-LLZO nanofibers. **Figure 2a** depicts a field emission-scanning electron microscopy (FE-SEM) micrograph of as spun Al-LLZO ceramic nanofibers. The as-prepared sample has a consistent distribution of Al-LLZO nanofibers with diameters ranging from 80 to 150 nm. The sample calcined at 600 °C displays Al-LLZO nanofibers with porous microstructures with a more or less homogenous distribution (Figure 2b). The nucleation and growth of the Al-LLZO ceramic crystal fibers network broaden the shape and diameters of the fibers. The surface morphology of Al-LLZO nanofibers is disrupted when the

sintering temperature is gradually increased to 700–800 °C (Figure 2c,d). The low-temperature calcination results in interconnected porous nanofibers, but high-temperature sintering results in significantly less porous 3D nanofibers; as a result, the nanofibers are intertwined. Furthermore, the formation of ceramic Al-LLZO nanofibers sintered at 800 °C is ensured by transmission electron microscopy (TEM) and selected area electron diffraction (SAED) pattern analysis, shown in Figure 2e,f. It indicates that electrospun fibers calcined at high temperatures show a uniform dispersion of short 3D fibrous networks. The interplanar distance ( $d$ ) was calculated from the SAED pattern as described in the literature.<sup>[26,27]</sup> The interplanar distances of the Al-LLZO determined by SAED are 0.424, 0.285, and 0.163 nm, corresponding to the diffraction peaks at  $2\theta = 16.67^\circ$ ,  $30.8^\circ$ , and  $52.68^\circ$  and their crystallographic planes (112), (024), and (246). The  $d$  values obtained from SAED are comparable to that obtained from XRD, which ensured the formation of cubic Al-LLZO ceramic nanofibers.

The HPEs were synthesized by incorporating different compositions of cubic structure Al-LLZO ceramic nanofibers (calcined at 800 °C) into the PVDF/LiTFSI (SPE) polymer salt. **Figure 2g** depicts the effect of highly crystalline Al-LLZO nanofibers on the structural characteristics of SPE. It exhibits a typical XRD peak at  $2\theta = 20.5^\circ$  due to the 110/200 reflection of the  $\beta$ -phase PVdF,<sup>[28]</sup> as well as a peak at  $2\theta = 18^\circ$  and a broad hump about  $2\theta = 40^\circ$  assigned to the  $\gamma$  phase PVdF<sup>[29]</sup> in the HPEs. The introduction of 5 wt% Al-LLZO into the SPE disrupts the semicrystalline

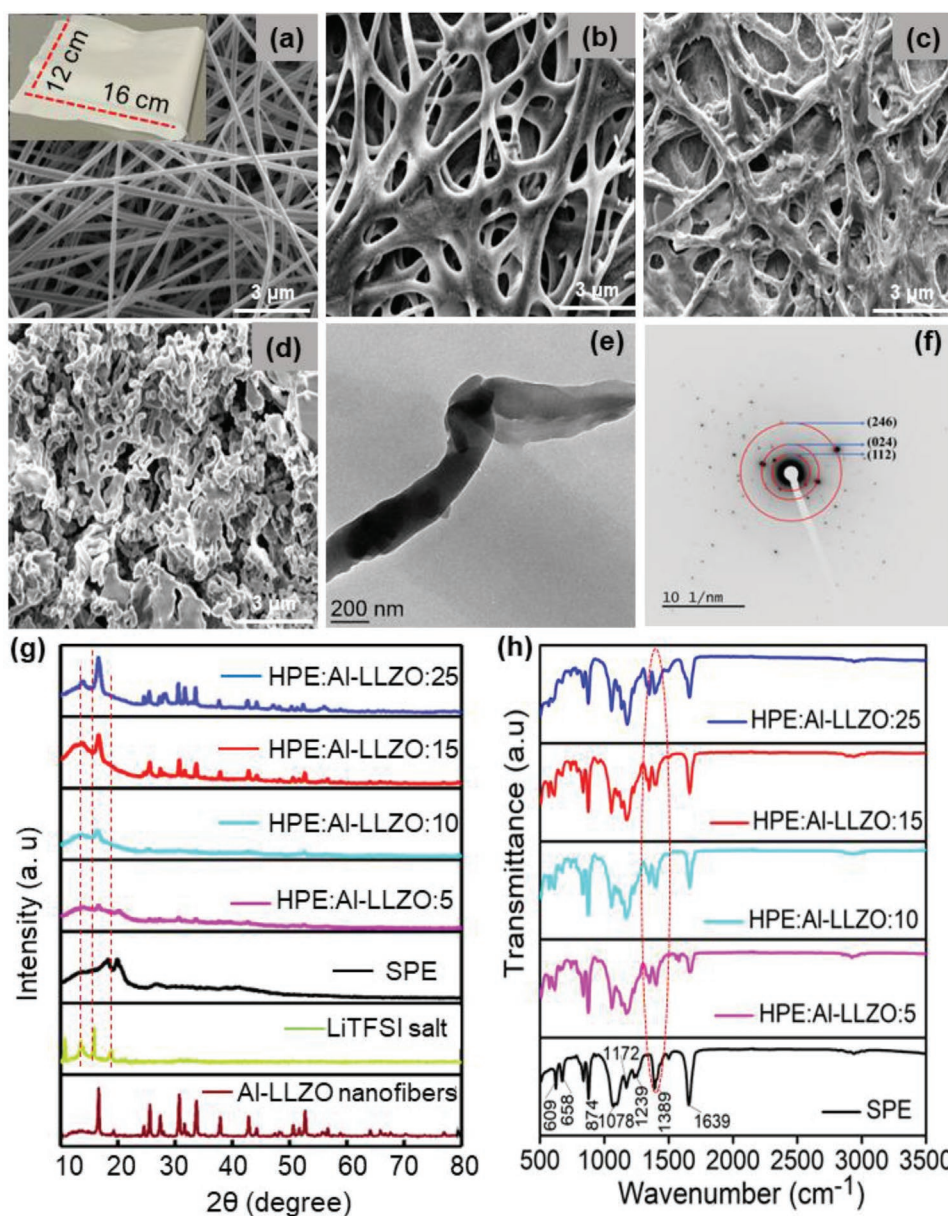


**Figure 2.** a) FE-SEM micrographs of the as-spun Al-LLZO nanofibers, b) calcined at 600 °C, c) 700 °C, and d) 800 °C for 3 h. e) TEM image and f) SAED pattern of Al-LLZO ceramic nanofibers calcined at 800 °C. g) XRD and h) FTIR spectra of SPE and HPE with different composition of Al-LLZO ceramic nanofibers.

structure of the PVDF host and reduces the crystalline peaks of PVDF. The peak owing to PVDF crystalline is entirely suppressed as the concentration of Al-LLZO nanofibers increases, but the peak due to the highly ionic conductive cubic phase of Al-LLZO increases as the concentration of ceramic nanofibers increases. The 15 wt% Al-LLZO added HPE has fewer crystalline peaks than the 25 wt% Al-LLZO HPE without any polymer and salt peaks, indicating a synergetic interaction between polymer and nanofiber fillers. The Al-LLZO reduces the crystallinity of the polymer matrix; when the Al-LLZO content exceeds 10 wt%, the SPE shows no crystalline peaks, confirming amorphization.

The crystalline peaks of LiTFSI salts ( $2\theta = 10.70^\circ$ ,  $13.60^\circ$ ,  $15.87^\circ$ , and  $18.93^\circ$ ) do not significantly emerge in the SPE and

5, 10, and 15 wt% Al-LLZO added HPE membranes, suggesting that the salt and polymer/Al-LLZO are perfectly complex. However, at high composition of Al-LLZO, a small peak observed at  $2\theta = 13.74^\circ$  is due to crystalline phase of salt. The Fourier transform infrared spectroscopy (FTIR) analysis was used to evaluate the interaction between ceramic nanofibers and polymer/salt matrices (Figure 2h). The SPE demonstrates the vibrational peak at  $1078\text{ cm}^{-1}$  caused by the asymmetric stretching vibration of the C–C backbone in PVDF polymer.<sup>[25]</sup> The vibrational modes observed at  $1172$  and  $1239\text{ cm}^{-1}$  are attributed to the asymmetric stretching of the  $\text{CF}_2$  and C–C bonds.<sup>[30]</sup> The peak observed at  $609$  and  $874\text{ cm}^{-1}$  are due to  $\text{CF}_2$  bending and the amorphous phase of  $\beta$ -phase,<sup>[24,28]</sup> and

the deformation vibration of  $\text{CH}_2$  originated at  $1389\text{ cm}^{-1}$ .<sup>[31]</sup> The bands originated at  $658$  and  $1639\text{ cm}^{-1}$  are attributed to the  $\text{S}=\text{O}$  stretching and LiTFSI aggregation.<sup>[32]</sup> The characteristic vibrational peaks of the PVDF/LiTFSI ( $1389$  and  $1078\text{ cm}^{-1}$ ) are shifted toward the low-frequency region, the intensity of peaks related to  $\text{CF}_2$  and  $\text{C}-\text{C}$  vibrations changes, and the emergence of a peak at  $1419\text{ cm}^{-1}$  after the addition of Al-LLZO nanofibers into SPE, suggesting a significant interaction between the Al-LLZO and PVDF/LiTFSI matrices. The intermolecular interaction of Al-LLZO nanofibers and PVDF weakened the crystalline properties of the PVDF polymer chains. Furthermore, the peak associated with LiTFSI agglomeration changed from  $1639$  to  $1658\text{ cm}^{-1}$ , and its intensity variation in HPEs, implying that the insertion of cubic Al-LLZO ceramic nanofibers promotes  $\text{Li}^+$  TFSI $^-$  dissociation and hence increases the free Li-ions in the HPEs.<sup>[32,33]</sup>

## 2.2. Ionic Conductivity, Thermal and Mechanical Stability

Impedance spectroscopy was used to examine the ionic conductivity of SPE and HPEs by placing the membranes between stain-less steel blocking electrodes in a Swagelok cell at room temperature. The Nyquist plots of SPE and HPEs are shown in **Figure 3a,b**. All the samples show a high-frequency semicircle with a low-frequency spike, clearly distinguished by Nyquist admittance (Figure S4a, Supporting Information). The depressed semicircle at high frequencies is caused by the bulk resistance of SPE and HPEs, whereas the tilted spike at low frequencies is due to electrolyte/contact electrode blocking.<sup>[34]</sup>

The bulk resistance ( $R_b$ ) of membranes can be calculated at the intersection of the semicircle on the real ( $Z'$ ) axis in the low-frequency zone,<sup>[31]</sup> but this method does not yield the exact bulk resistance if the Nyquist plots show a depressed semicircle, particularly if the Al-LLZO concentration exceeds  $10\text{ wt}\%$ . Hence, more accurate bulk resistance of SPE and HPEs can be obtained by theoretically fitting the Nyquist plots with an equivalent circuit model using EC lab software (Figure S4b, Supporting Information). The fitted resistance values and calculated ionic conductivity (using Equation (1)) of the SPE and HPEs are presented in Table S2, Supporting Information.

The bulk resistance of HPEs reduces as the concentration of Al-LLZO increases up to  $15\text{ wt}\%$  while it increases beyond  $15\text{ wt}\%$  (Figure 3c). The conductivity of the  $15\text{ wt}\%$  Al-LLZO integrated HPE is  $1.712 \times 10^{-4}\text{ S cm}^{-1}$  at  $25\text{ }^\circ\text{C}$ , which is two orders of magnitude greater than the SPE membrane ( $1.702 \times 10^{-6}\text{ S cm}^{-1}$ ). It demonstrates that  $15\text{ wt}\%$  Al-LLZO is the optimal concentration for improving the structural and electrical properties of HPEs. Well-dispersed interconnected Al-LLZO ceramic nanofibers reduce the degree of crystallinity of PVDF by disrupting its regular chain arrangements thereby expanding free volume and increasing the proportion of amorphous phase. The Li-ions move freely through the enhanced free volume or flexible-amorphous phase of the PVDF host. As a result, the enriched amorphous phase of PVDF improves the polymer's chain segment mobility, resulting in a higher ion conductivity than crystalline polymer. Furthermore, the interconnected Al-LLZO in the polymer/salt complex improved salt dissociation and served as pathways for rapid Li-ion transport. The Al-LLZO serves as a conductive network

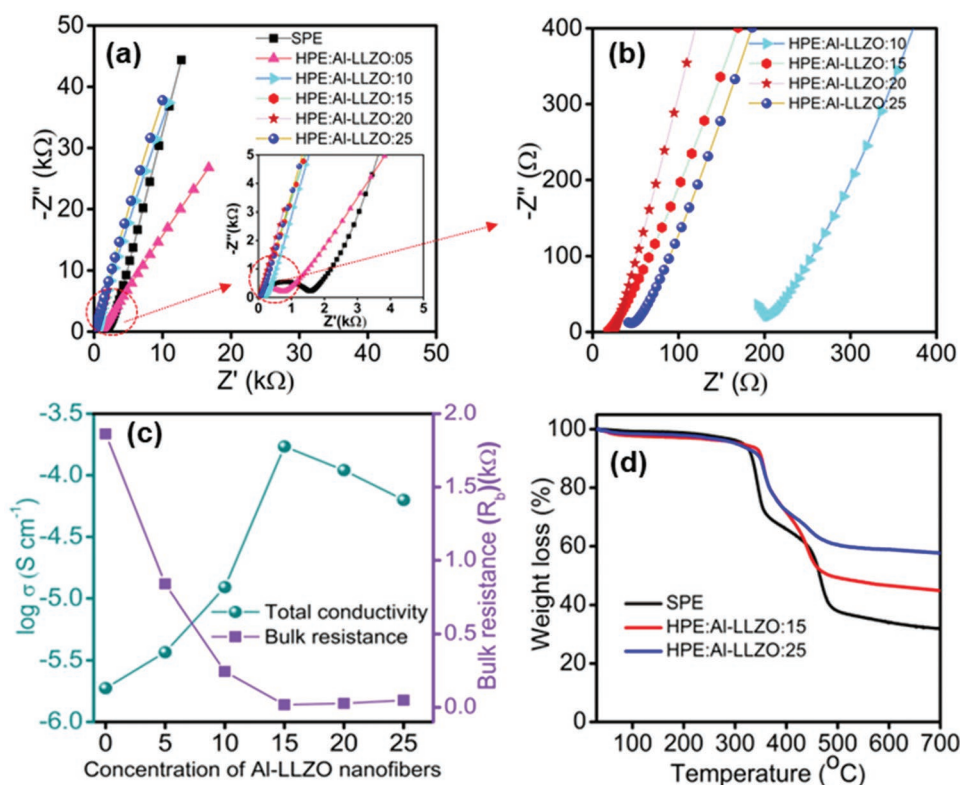


**Figure 3.** a,b) Nyquist plots of SPE and HPEs at room temperature measurement, c) conductivity versus concentration of Al-LLZO ceramic nanofibers, and d) TGA curves of SPE and HPEs.

with negligible grain boundary resistance within the complex polymer matrices. The ceramic nanofibers also accelerate the dissociation of  $\text{Li}^+ \text{TFSI}^-$  ion pairs via Lewis acid/base interactions, resulting in higher concentrations of mobile Li-ions and hence increased ionic conductivity.<sup>[16,35]</sup> The crystalline phase of Al-LLZO acts as additional conduction channels, which is beneficial for enhancing ionic conductivity. Taking into account the contributions of the enhanced amorphous phase and continuous ionic transport channels of Al-LLZO ceramic nanofibers, the HPE demonstrated higher ionic conductivity than the SPE. The TGA analysis was used to infer the thermal stability of the SPE and HPEs, as shown in Figure 3d. The thin SPE and HPE films heated twice at high vacuum result in no significant weight loss of solvent and moistures between the temperatures 25–300 °C. The two-step heating method is adequate to remove the solvent from the thin SPE and HPEs films. The weight loss of the LiTFSI salt at 360–470 °C (Figure S5a, Supporting Information) demonstrates salt decomposition. The considerable weight loss observed between 320 and 400 °C and 410–520 °C due to salt and salt/polymer degradation. The weight was remaining from HPEs containing 15 and 25 wt% Al-LLZO after heating at 550 °C is 45.5 and 57.41 wt%, respectively. The results show that the HPEs have good thermal stability (Figure 3d and Figure S5b,c, Supporting Information) which can be used in high-temperature lithium batteries.

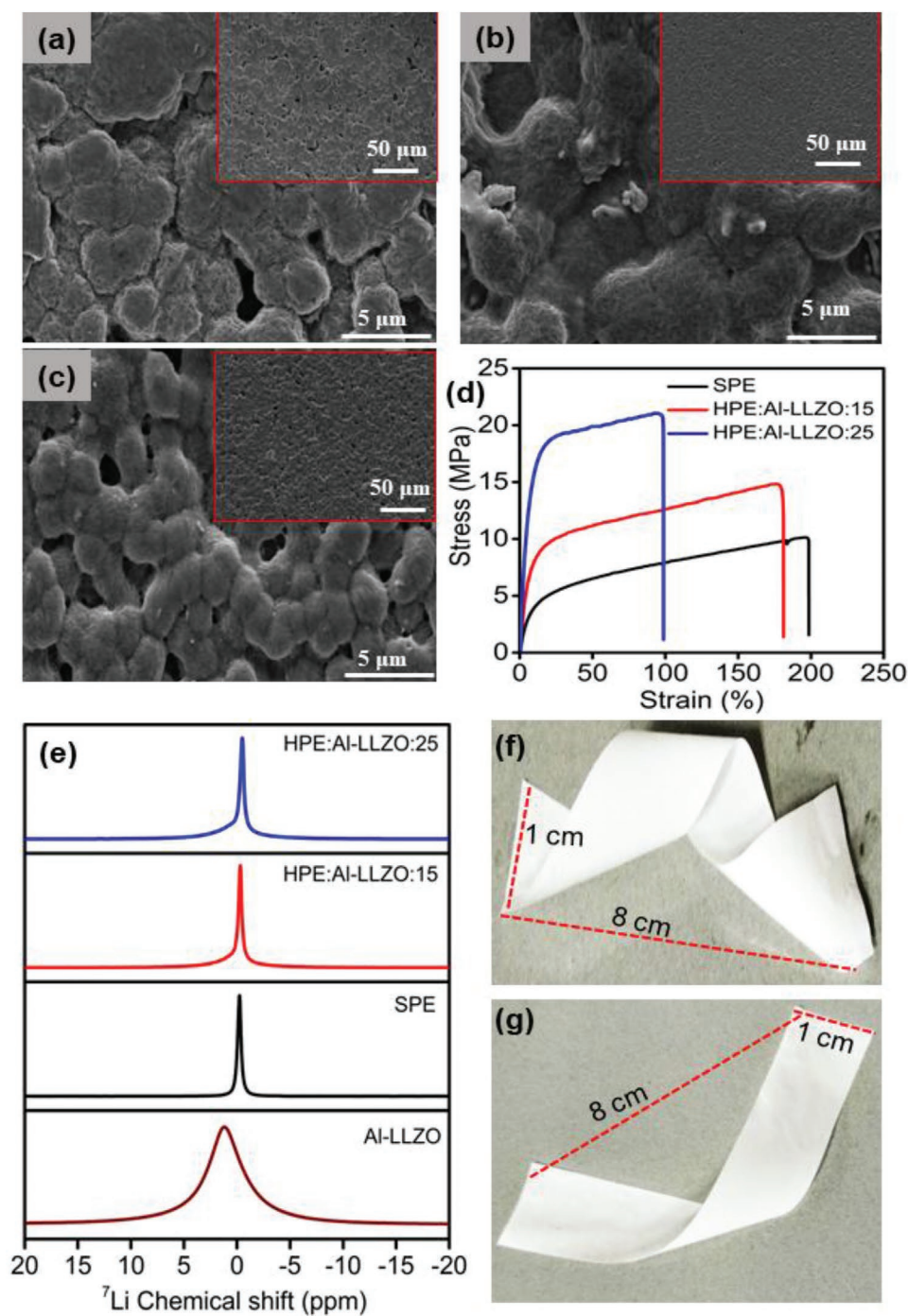
According to the structural, optical, electrical, and thermal properties of HPEs, 15 wt% Al-LLZO is optimized; hereafter, the present work has focused on investigating the electrochemical performance of 15 wt% Al-LLZO incorporated HPE in comparison with SPE and high concentration of ceramic nanofibers (25 wt%). Thermal shrinkage and flame-retardant performance of SPE and HPEs are shown in Figure S5b,c, Supporting Information. When the temperature is raised above 150 °C, the SPE sample suffers from severe volume shrinking (Figure S5b, Supporting Information). The change in volume and shape of the solid electrolyte membrane causes direct contact between the cathode and anode, resulting in a short circuit and significant capacity fading. The HPEs possess enhanced thermal shrinkage behavior even at high temperatures (200 °C), an essential feature of solid polymer electrolytes for tuning the cycle life of SSBs. The flame test was carried out multiple times to confirm the flame retardancy of SPE and HPEs as shown in Figure S5c, Supporting Information. In comparison to HPEs, the SPE has limited thermal stability and began to burn and produce smoke within 1 s of coming into contact with an ignited lighter. Even after several seconds, the HPEs exhibit excellent heat stability, with most of the membranes remaining intact. The HPE:Al-LLZO:25 has much better flame retardancy than HPE:Al-LLZO:15, and the low flammability of HPEs provides good safety for Li-metal batteries and SSBs.

Figure 4a–c, depicts the surface morphology of free-standing SPE, and HPEs, in which the SPE shows a non-uniform sphere-like rough surface morphology with many micropores and cavities of PVDF/LiTFSI particles (Figure 4a) limiting Li-ion transport and reducing ionic conductivity. The HPEs also have a sphere-like morphology that is more homogeneous than SPE, with no visible cavities or micropores. The difference in the surface morphology of SPE and HPE are attributed to the incorporation of Al-LLZO ceramic nanofibers into SPE which

interconnects the microparticles of the PVDF/LiTFSI complex and fuses the micro-voids, resulting in the uniform and densified microstructures of HPEs (Figure 4b,c). The uniform distribution of interlinked ceramic nanofibers and polymer matrix with no defects enables rapid Li-ion transportation and diffusion, increasing polymer electrolyte's ionic conductivity.<sup>[16]</sup> The mechanical strength and flexibility of a solid polymer electrolyte are essential in improving the safety and durability of SSBs in long-term operation. Figure 4d depicts the stress–strain curves of SPE and HPEs; the tensile strength of SPE is found to be 10 MPa, and the strain around 200%. The addition of 15% Al-LLZO ceramic nanofibers to SPE improves tensile strength from 10 to 15 MPa, and strain is  $\approx$ 179%. Furthermore, the flexibility and mechanical performance of HPE (15 wt%) were examined by lifting loads of 250 and 542 g using a membrane with dimensions of 1 cm  $\times$  8 cm (width and length), as shown in Figure S6a–c, Supporting Information, (photographs). The HPE can endure the same size and shape before and after lifting the load (Figure S6c, Supporting Information). The bent and twisted HPE shows good flexibility (Figure 4f,g). The superior mechanical strength and flexibility of HPE (15 wt%) are due to the homogeneous distribution of highly conductive unique short 3D Al-LLZO ceramic nanofibers and the strong adhesive effect between ceramic nanofibers and PVDF polymer matrix.<sup>[9]</sup> The obtained tensile strength (14.88 MPa) and strain (179%) of HPE are significantly higher than many recent reports.<sup>[9,16,17,33]</sup> The significant improvement in mechanical strength and elastic qualities will allow the HPE to have excellent stability at low membrane thickness and good lithium dendrite suppression capability. The higher concentration (25 wt%) of Al-LLZO results in greater tensile strength of 21.05 MPa but a lower strain (96%) than SPE and HPE (15 wt%); this poor elastic performance affects the flexible operation of SSB. Solid-state  $^7\text{Li}$  NMR is a powerful tool for inferring the chemical environment of Li-ions and transport pathways, as shown in Figure 4e. The  $^7\text{Li}$  NMR (30 kHz) signals observed at 1.2, 0.2, 0.3, and 0.5 ppm indicate the presence of Li-ions in the Al-LLZO ceramic nanofibers, SPE, and HPEs membranes, respectively.<sup>[36,37]</sup> The  $^7\text{Li}$  NMR signal of SPE (0.2 ppm) shifted to 0.3 and 0.5 ppm when 15 and 25 wt% Al-LLZO were added to SPE, indicates the addition of ceramic fillers can reduce the crystallinity of polymer and salt which in turn increases the disorder of Li-ion local environments within polymers, manifested as shifted resonances in  $^7\text{Li}$  NMR. The finding demonstrates, the formation of a complex between Al-LLZO ceramic nanofibers and PVDF/LiTFSI, implying that the Al-LLZO-polymer matrix interface provides an additional Li-ion conduction pathway, thereby increasing the ionic conductivity of HPE.

### 2.3. Electrochemical Stability and Li Transference Number

The Li-ion transference number ( $t_{\text{Li}^+}$ ) has been used to examine the ion transport performance of an electrolyte, and the chronoamperometric polarization curves of SPE and HPE are shown in Figure 5a–c. The  $t_{\text{Li}^+}$  was calculated using Equation (2), and it is observed that the HPE with 15 and 25 wt% Al-LLZO exhibits the  $t_{\text{Li}^+}$  value of 0.720 and 0.715 which is higher than SPE (0.157) and conventional liquid electrolyte ( $\approx$ 0.2 to



**Figure 4.** FE-SEM micrographs of a) SPE, b) 15 wt%, and c) 25 wt% Al-LLZO incorporated HPEs. d) Stress–strain curves. e) <sup>7</sup>Li NMR spectra of Al-LLZO ceramic nanofibers, SPE, and 15 and 25 wt% Al-LLZO incorporated HPEs. f, g) Bent and twisted elastic performance of HPE with 15 wt% Al-LLZO membranes.

0.35).<sup>[9,16]</sup> The low transference number is due to the intense polarization in the SPE electrolytes. Anion migration is more significant in the SPE, lowering the transference number. The transference number of SPE determined in this work is similar to that reported in the literature for PVDF/LiTFSI-based systems ( $t_{Li^+} = 0.16$ ).<sup>[17]</sup>

The enhancement of  $t_{Li^+}$  HPEs is attributed to the inherent Li-ion conductivity of Al-LLZO ceramic nanofibers, strong interaction between TFSI<sup>-</sup> and Al-LLZO ceramic nanofibers as evidenced by intensity variation and shift in the FTIR vibrational mode observed at 1659 cm<sup>-1</sup> (Figure 2h), and enhanced segmental motion of polymer chains arising from



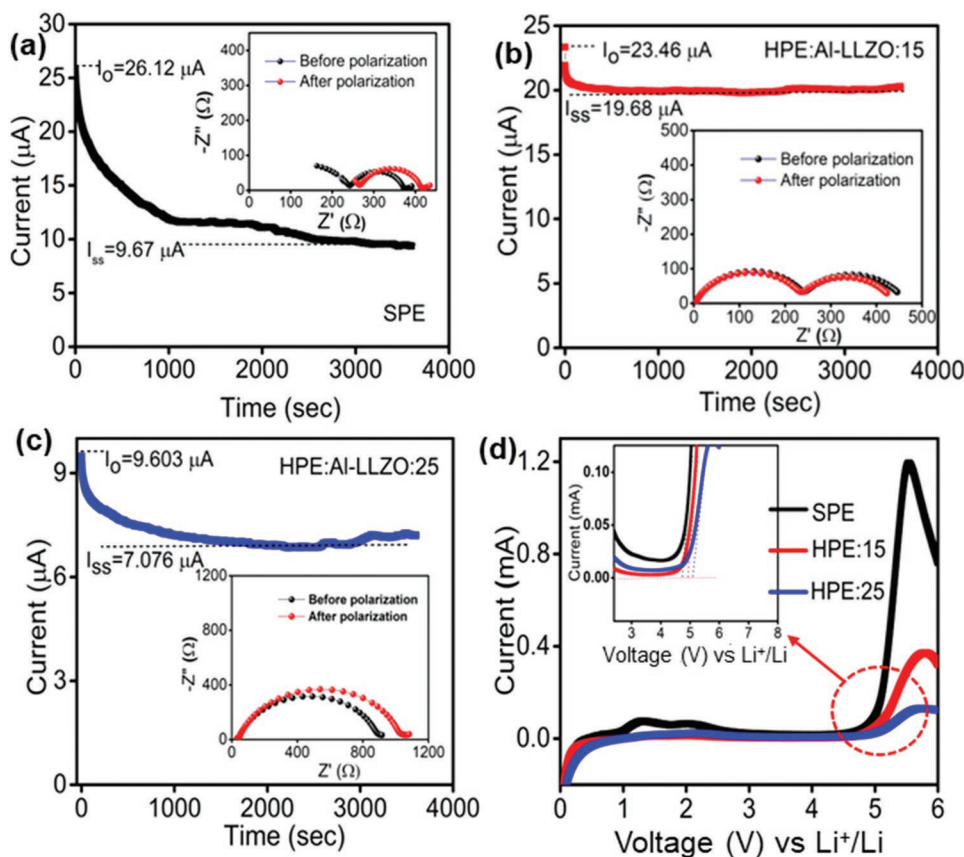


**Figure 5.** a–c) Chronoamperometric polarization curves, electrochemical impedance spectra before and after polarization (inset pictures), and d) linear sweep voltammetry curves of SPE and HPEs.

the amorphous phase of PVDF. The high  $t_{Li+}$  value of HPE facilitates smooth Li-ion transportation, limiting space charge layer influence and producing a uniform Li-ion concentration for good Li-ion stripping/plating performance. Furthermore, a slight fluctuation in polarization resistance before and after a steady state (Figure 5b, inset) indicates that the HPE (15 wt%) is more stable in the presence of Li metal batteries. The linear sweep voltammetry (LSV) was used to determine the electrochemical stability of SPE and HPE membranes, as illustrated in Figure 5d. The electrochemical stability window of the SPE and HPEs containing 15% and 25% Al-LLZO are 4.90, 5.01, and 5.12 V, respectively. The wide electrochemical stability window allows HPEs to be used in high voltage SSB batteries.

#### 2.4. Li Symmetric Cell Dendrite Tests

Dendrite formation during charge–discharge is a crucial concern with lithium metal-based anode SSBs. Dendrites are formed as a result of the non-uniform deposition of Li, which penetrate the weak electrolyte and short circuit the battery. The interface stability of anode/electrolyte of the best performing free standing HPE with 15 wt% Al-LLZO nanofibers was investigated by preparing the Li/HPE/Li symmetric cell and compared it to the SPE symmetric cell (Li/SPE/Li). **Figure 6a** depicts the galvanostatic charge–discharge profile of SPE and

HPE symmetric cells over 700 h at 25 °C at different current densities of 0.25, 0.5, 1, 2, and 4 mA cm<sup>-2</sup>. The SPE symmetric cell has a stable polarization potential of 128 mV with a coulombic efficiency of 87.5% over 100 h at 0.25 mA cm<sup>-2</sup>. When the current density is increased to 0.5 mA cm<sup>-2</sup>, the polarization voltage increases with the number of repeated cycles and short-circuits after 216 h. The SPE symmetric cell displays an arc-shaped charge–discharge profile (Figure 6b) with a low coulombic efficiency, which is attributed to dendritic and dead Li accumulation.<sup>[38]</sup> The SPE and HPE exhibit the overpotential of 520 and 11.7 mV after 250 h at 0.5 mA cm<sup>-2</sup> (Figure 6c), and the large degree of polarization arising from severe Li-dendrite nucleation and growth at the anode/electrolyte interface.<sup>[38]</sup> The plating/stripping of a Li/HPE/Li symmetric cell reveals uniform charge–discharge plateau profiles over 700 h with current densities ranging from 0.25 to 4 mA cm<sup>-2</sup>. At high current density, the HPE delivered stable and uninterrupted cycles with polarization voltage of 35 mV and 99.9% coulombic efficiency (Figure 6d) (4 mA cm<sup>-2</sup>).

The HPE symmetric cells were continuously charged and discharged at a high current density of 7 mA cm<sup>-2</sup> for 1050 h, as presented in Figure 6e. It showed that the HPE has excellent lithium stripping/plating performance, with no short circuits occurring after 1050 h of operation without voltage fluctuations (Figure 6g) and the polarization potential remaining stable at 79 mV (Figure 6f).

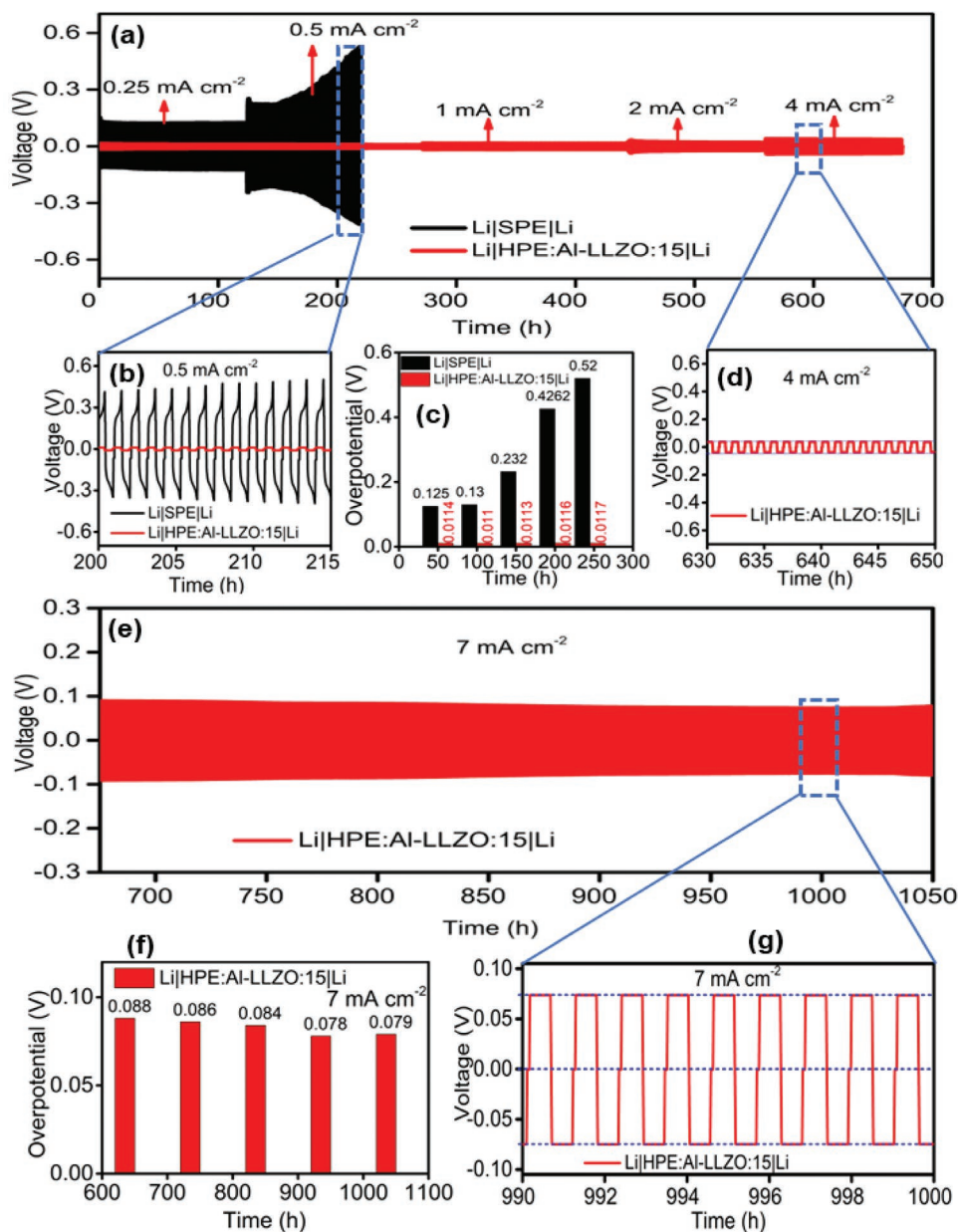


**Figure 6.** a) Galvanostatic cycling performance of Li|SPE|Li and Li|HPE:Al-LLZO:15|Li symmetric cells at different current densities of 0.25, 0.5, 1, 2, and 4 mA cm<sup>-2</sup>. b) GCD profile of SPE with test duration of 200–215 h. c) Comparison of overpotential versus test duration at 0.25 and 0.5 mA cm<sup>-2</sup>. d) GCD profile of HPE versus time (630–650 h). e) GCD profile of HPE symmetric cells continued up to 1050 h at a high current density of 7 mA cm<sup>-2</sup>. f) Comparison of overpotential of HPE at 7 mA cm<sup>-2</sup> and g) GCD profile of HPE versus time (990–1000 h).

The incorporation of Al-LLZO ceramic nanofibers significantly improved the  $t_{Li+}$ , which facilitates the uniform deposition of Li on anode, hindering the nucleation and growth of dendrites. The Al-LLZO offers excellent mechanical strength and flexibility to HPE, providing enough strength to suppress dendrite formation throughout the charge–discharge process. Moreover, the Al-LLZO ceramic nanofibers have a good affinity with the PVDF polymer matrix, which limits ion aggregations at the anode-electrolyte interface and enables uniform distribution of ions at the solid–solid interface, resulting in good Lithium stripping/plating performance over long cycle life. According to the findings, the Al-LLZO ceramic nanofibers

can effectively reduce interfacial resistance at solid–solid interfaces, allowing for ultra-stable Li plating and stripping cycles. The polarization potential (11.7, 36.8, and 79 mV at 0.5, 4, and 7 mA cm<sup>-2</sup>) reported in this work is much lower than numerous previous studies<sup>[7,9,16,17,33,39]</sup> and those studies were conducted the stripping/plating performance at low current densities (0.5, 0.1 0.15, 0.2, 0.3, 1, and 2 mA cm<sup>-2</sup>). This work examined the stripping/plating performance at high current density, which is significant for evaluating dendrite growth. The results showed that Al-LLZO strongly regulates Li-ion deposition and facilitates the assembly of dendrite-free SSBs. According to the structural, morphological, thermal stability, ionic conductivity, and

electrochemical results, the composition of Al-LLZO ceramic nanofibers was optimized as 15 wt% in HPEs. Further, the optimized HPE was chosen for the interface-based core-shell design.

### 2.5. Interface-Based Core-Shell Structure and Room Temperature Solid-State Battery Performance

The poor surface contact and high thickness of free-standing solid electrolytes hinder the practical application of SSBs. The current work attempted to address these issues by designing a unique interface-based core-shell structure via direct integration of the optimized composition 15 wt% Al-LLZO ceramic nanofibers incorporated HPE on the porous cathode (HPEIC), as shown in Figure 7a (photograph of HPEIC). In three steps, the ultrathin HPE was coated on the cathode electrode using an optimum slow evaporation process. Figure 7b depicts FE-SEM

cross-sectional micrographs of HPEIC; the thickness of ultrathin HPE on porous LFP cathode particles is found to be  $\approx 7 \mu\text{m}$  which is the thinnest layer of solid electrolytes ever used in SSBs. Even though the coated electrodes were calendared, the surface porosity of cathode particles could not be eliminated 100%<sup>[40]</sup> (Figure 7c). As a result, the direct integration of HPE on the cathode electrode can fill the pores and micro-voids during solvent evaporation while simultaneously acting as an interface-based core-shell. The porous LFP cathode particles are encased in HPE networks, which shield the active cathode particles and provides a superior cathode/electrolyte solid-solid interface contact.

The LFP cathode particles serve as the core, and the wrapped HPE as the shell, resulting in the interface-based core-shell structure (Figure 7d). The cross-sectional EDS mapping of the HPEIC is depicted in Figure S7, Supporting Information, which ensures the formation of HPEIC. The flexibility of the integrated electrolyte-cathode was investigated by folding,

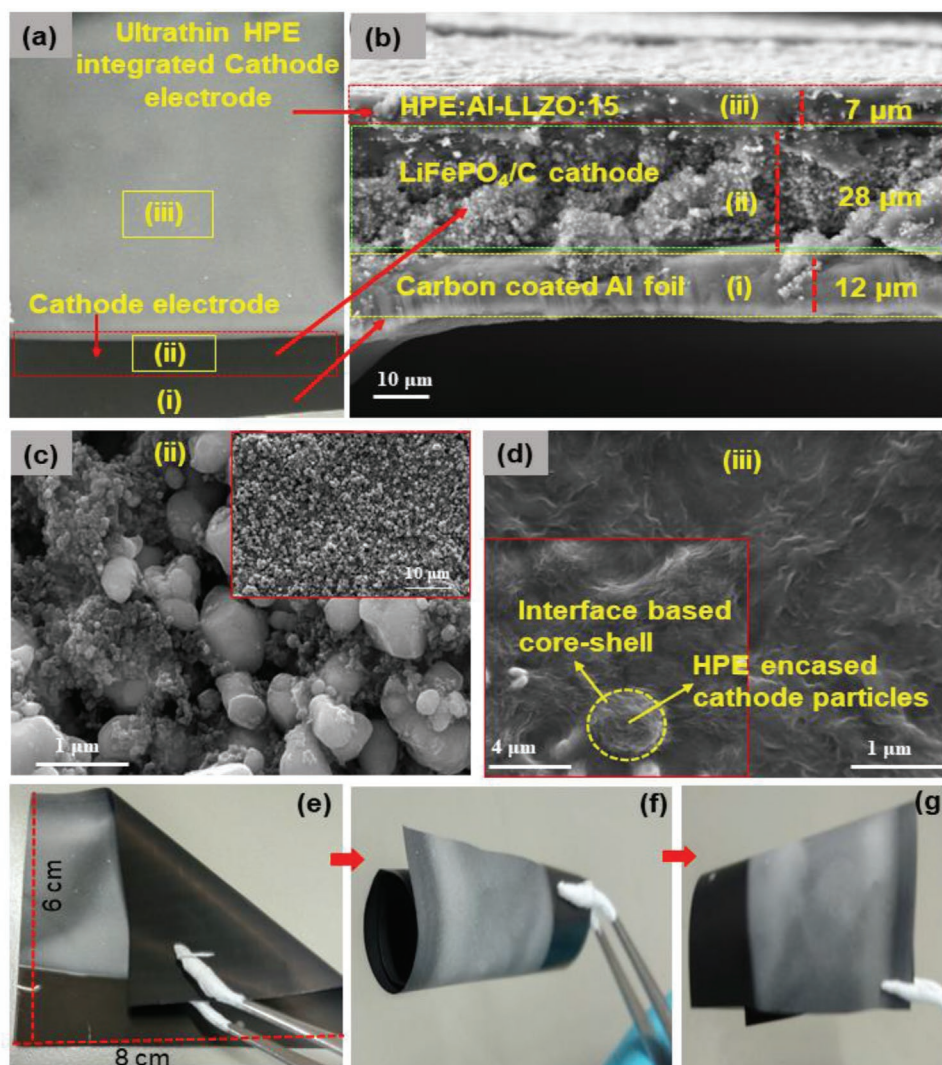


**Figure 7.** a) Photograph of HPE integrated LFP cathode. b) Cross-sectional FE-SEM micrograph of interface-based core-shell HPE integrated LFP cathode. FE-SEM micrographs of the surface of c) cathode coated electrode, d) HPE encased LFP interface-based core-shell structure, and e–g) photographs of folded, rolled, and bent HPEIC.

rolling, and bending HPEIC, as shown in Figure 7e–g. The HPEIC demonstrates great flexibility even after being folded, rolled, and bent numerous times, indicating that the rational design of HPE on the cathode electrode offered excellent flexibility, cathode particle binding, and elastic performance of the cathode electrodes. The unique characteristics of HPEIC hinder the cathode particle cracking during the charge–discharge process and enable to design of highly flexible SSBs. Furthermore, the unique design of interface-based core–shell HPEIC offers ultrathin solid electrolyte, an excellent cathode/electrolyte interface contact, good flexibility, facilitates sound Li-ion diffusion, and smooth binding of inter particles of cathode material.

The CR30322 coin cell type SSBs were fabricated to test the practical applicability of the solid-state HPEIC and compare its battery performance to that of free-standing SPEs and HPEs. The conventional SSBs were assembled by stacking individual components such as the Li-metal anode, the LFP cathode, and free-standing SPE and HPEs (15 and 25 wt% Al-LLZO). At the same time, the integrated SSB was fabricated by combining the interface-based core–shell HPEIC and the Li-metal anode and tested their battery performance at 25 °C. The electrochemical impedance spectroscopy (EIS) was used to elucidate the charge transfer characteristics and Li-ion diffusion in SSBs, as shown in Figure 8a,b. The EIS plots of the activated cells show a high-frequency semicircle and a low-frequency inclined line. The high-frequency semicircle is related to the charge transfer resistance. The low-frequency inclined line is attributed to the Warburg diffusion of the active material, which is associated with the Li-ion transport kinetics over the electrode.<sup>[16,34]</sup> The EIS plots were fitted using the equivalent circuit model (Figure 8a, inset shows the most suited equivalent circuit model). The  $R_e$  represents bulk resistance, and  $R_{ct}$  is the charge transfer resistance between solid electrolyte and electrodes, respectively.

Further, the internal resistance (IR) of the activated SSBs was measured using Arbin battery tester by applying the pulse current amplitude 6  $\mu$ A, width 50 msec, and offset 0A conditions. The IR and charge transfer resistance of SPE, HPEs, and HPEIC SSBs are presented in Table S3, Supporting Information. In comparison to free-standing SPE and HPEs, the HPEIC has relatively low charge transference resistance (74.2  $\Omega$ ) and internal resistance (44  $\Omega$ ), which is attributed to the good interfacial contact between the HPEIC and electrodes.

The lithium-ion diffusion coefficient ( $D_{Li^+}$ ) of the active material was calculated using the Equations (S1) and (S2), Supporting Information, (more details about the  $D_{Li^+}$  calculation are provided in the supporting information) and presented in Table S4, Supporting Information. The effective design of the interface-based core–shell via integration of HPE on the porous cathode significantly increases the lithium-ion diffusion coefficient from  $1.65 \times 10^{-14}$  to  $3.63 \times 10^{-12}$   $\text{cm}^2 \text{s}^{-1}$ , which is two orders of magnitude higher than that of free-standing SPE and HPEs electrolytes used in the fabrication of SSBs. The determined lithium-ion diffusion coefficient is comparable to liquid electrolyte-based lithium-ion batteries (LIBs).<sup>[41]</sup> The integration of ultrathin HPE on the surface of the cathode not only improved the cathode/electrolyte interface contact but also enhanced the  $Li^+$  diffusion of the cathode electrode. The mechanism of the improved  $Li^+$  diffusion is indicated in the schematic diagram (Scheme 1b), where the highly ionic conductive

networks of HPEs encapsulate the cathode particles, facilitating excellent  $Li^+$  diffusion.

The galvanostatic charge–discharge (GCD) curves of conventional LFP|SPE|Li, LFP|HPE-Al-LLZO:15|Li, LFP|HPE-Al-LLZO:25|Li SSBs and HPEIC/Li SSB are depicted in Figure 8c–f. The initial specific discharge capacity of SPE, 15 and 25 wt% Al-LLZO embedded HPEs and HPEIC are found to be 125, 142, 123, and 166  $\text{mAh g}^{-1}$ , and after 5th cycle is 112, 134, 118, and 166  $\text{mAh g}^{-1}$  at 0.1 C rate, respectively. Although the HPE with 15% Al-LLZO outperformed the other samples in terms of structural, electrical, and electrochemical performance, it delivered a lower specific capacity than the HPEIC due to poor interface contact between the cathode and free-standing electrolyte. Figure 8g compares the cycling stability of the free-standing SPE, HPEs-based SSBs, and HPEIC SSB at 0.5 C for 120 cycles at 25 °C. The LFP|SPE|Li, LFP|HPE-Al-LLZO:15|Li, LFP|HPE-Al-LLZO:25|Li SSBs, and HPEIC/Li SSB exhibited the initial discharge capacity of 111, 118, 103, and 159  $\text{mAh g}^{-1}$  and 58, 90, 86, and 159  $\text{mAh g}^{-1}$  after 120 cycles. The HPEIC/Li SSB delivered excellent capacity retention of 100% after 120 cycles at 0.5 C, which is the first report to obtain 100% capacity retention (coulombic efficiency is 99.79%) after 120 cycles for LLZO-based CPEs. The HPEIC exhibits the best electrochemical performance in initial capacity and cycling stability at 25 °C than the reported value in the recent LLZO-based composite solid polymer electrolytes (Table S5, Supporting Information). Figure 9a,b depicts the rate capability of free-standing SPE, HPEs-based SSBs, and integrated HPEIC SSB. The rate performance was assessed by charging and discharging the SSBs for 6 cycles at each current rate. The integrated HPEIC/Li SSB delivered high capacities of 166.05, 163.04, 160.52, 145.26, 135.42, and 109.40  $\text{mAh g}^{-1}$  at 0.1, 0.3, 0.5, 1, 3, and 5 C, respectively. After performing the 1 C cycling, the rate was reduced to 0.1 C, and the specific capacity returned to 165  $\text{mAh g}^{-1}$ , demonstrating its good rate performance.

In comparison, the SSBs prepared with free-standing SPE and HPEs have low capacities at the same current rates due to large internal resistances and poor interface contact. The conventional SSBs assembly is incapable of supporting fast charging and rate capability. Figure 9c shows the long-term cycling life of an integrated HPEIC/Li cell at 0.5 and 1 C over 300 cycles at 25 °C. The HPEIC/Li cell provided a discharge capacity of 110  $\text{mAh g}^{-1}$  after 300 cycles at 1 C rate with the coulombic efficiency of 99.15%. The good cycling stability and rate capability of HPEIC/Li SSB with LFP cathode due to the low charge transfer resistance, internal resistance, good electrode/electrolyte interface conduct, and improved  $Li^+$  diffusion. The ceramic nanofibers eliminate grain boundaries at the interface with adjacent particles, providing much better charge transport and enhancing electrochemical performances.<sup>[42–44]</sup> The Al-LLZO ceramic nanofibers have a high surface-to-volume ratio and are uniformly distributed through the porous structure of the cathode electrode, filling the voids and porous in the cathode, significantly improving interface contact between the cathode and the electrolyte, and thus lowering the internal resistance of the SSB.

Furthermore, the battery performance of HPEIC was tested with NMC811 cathode material to ensure compatibility of the interface-based core–shell HPEIC for high voltage cathode

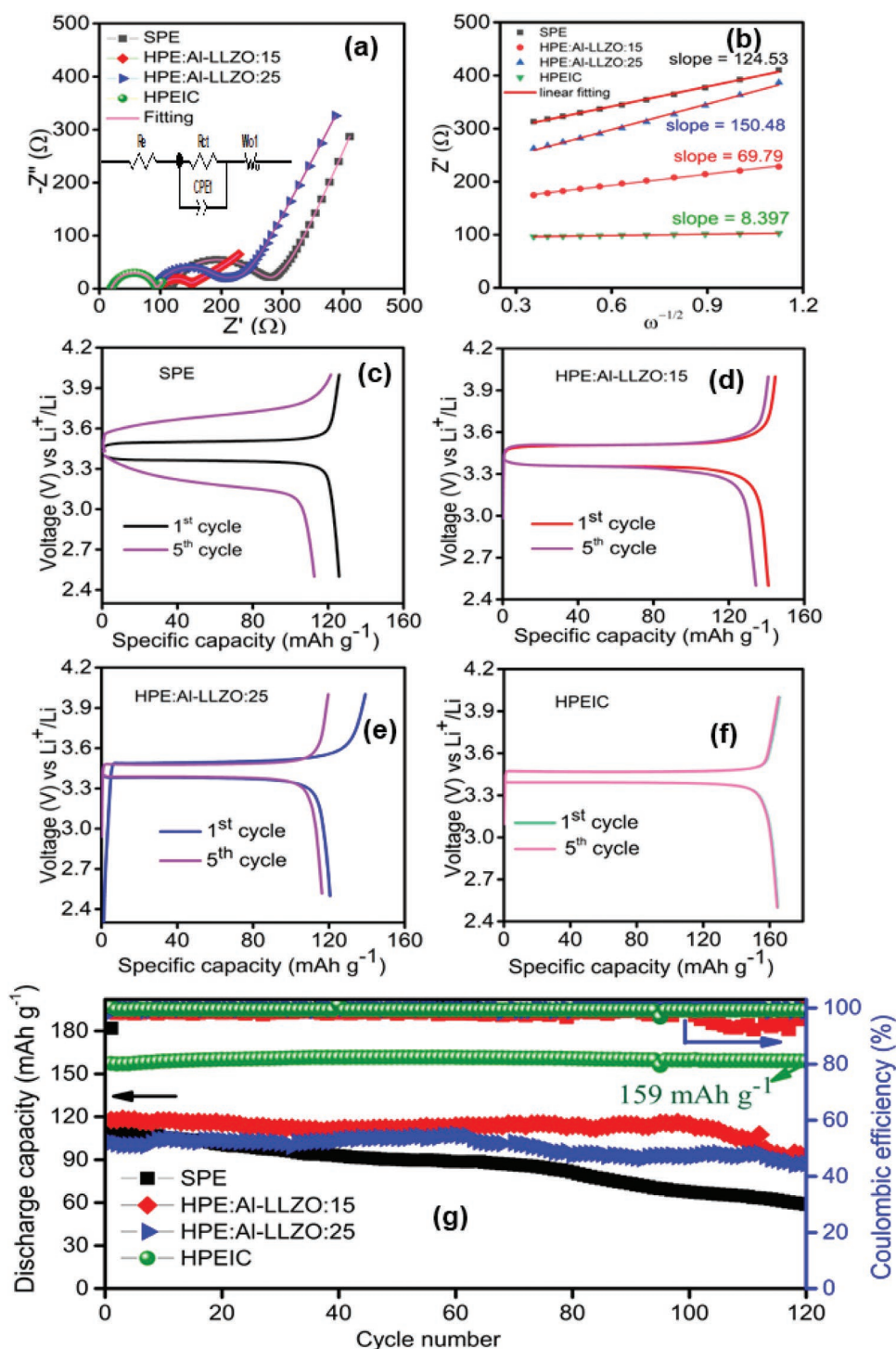


**Figure 8.** a) EIS plot and b) relation between  $Z_{real}$  versus  $\omega^{-1/2}$ . c–f) Galvanostatic charge–discharge curves of free-standing SPE, HPEs, and HPEIC at 0.1 C and g) cycling stability and coulombic efficiency of SPE, HPEs, and HPEIC SSBs at 0.5 C for 120 cycles.

material in the voltage range of 2.8–4.3 V. Figure 9d depicts the EIS of the activated HPEIC-NMC811|Li SSB, which has a charge transfer resistance of 54  $\Omega$ . As shown in Figure 9e, the HPEIC-NMC811|Li SSB presented the initial charge and discharge capacity of 255 and 250  $\text{mAh g}^{-1}$  (coulombic efficiency is 98.03%). It also delivered the 5th charge and discharge

capacity of 249 and 246  $\text{mAh g}^{-1}$ , with a coulombic efficiency of 98.79% at 0.1 C, which is comparable with conventional NMC811 cathode LIBs.<sup>[45,46]</sup> The cycling stability of HPEIC-NMC811|Li SSB was tested for 120 cycles at current rates of 0.5 and 1C (Figure 9g). The NMC811|Li cell had discharge capacities of 134 and 120  $\text{mAh g}^{-1}$  after 120 cycles at 0.5 and 1 C with capacity

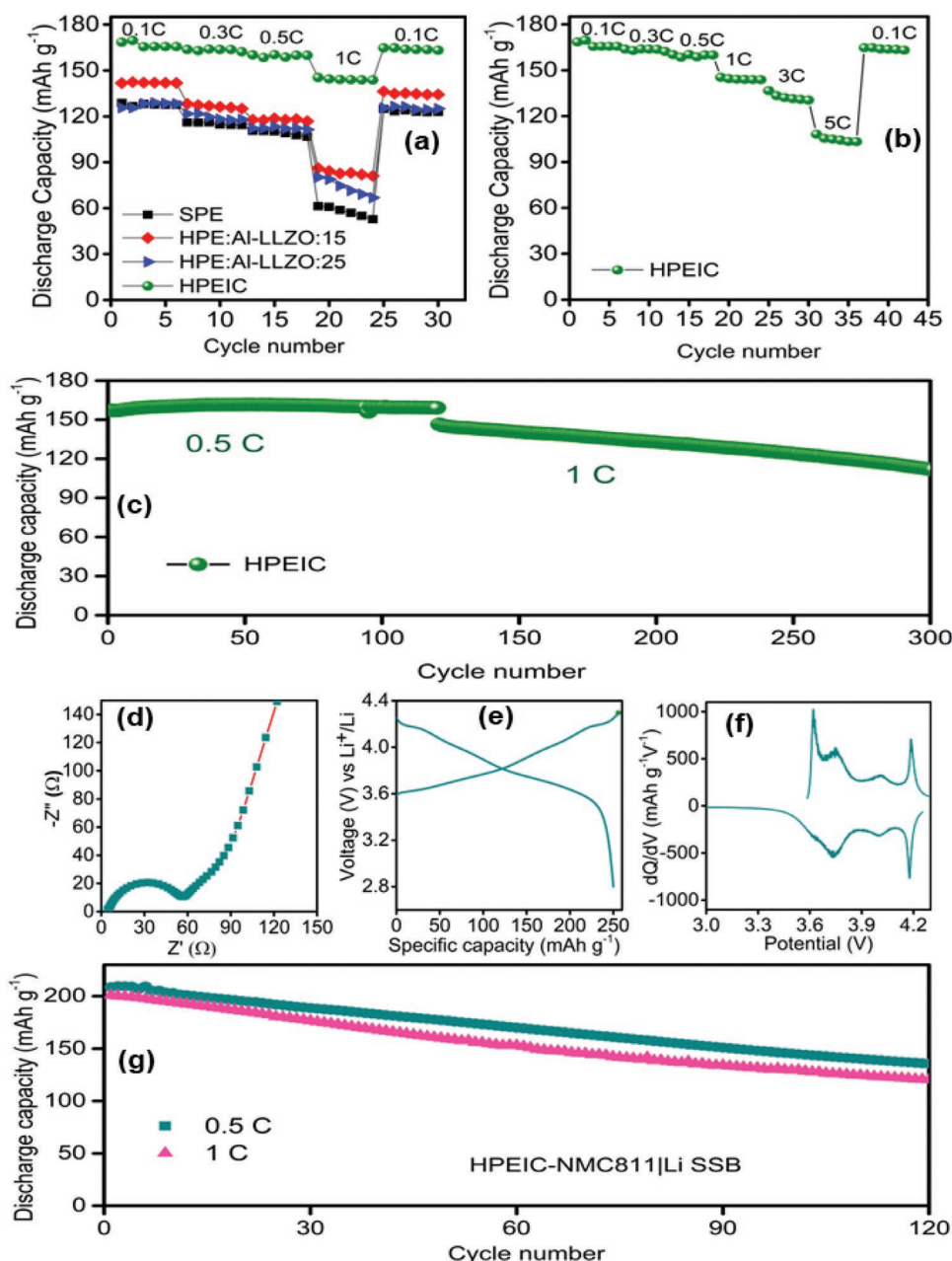


**Figure 9.** a) Rate capability of free-standing SPE, HPEs, and integrated HPEIC SSBs. b) Rate capability of integrated HPEIC SSB. c) Long-term cycle life of HPEIC SSB at 0.5 and 1 C rate over 300 cycles. Electrochemical performance of HPEIC with NMC811 cathode: d) EIS, e) initial charge–discharge curve, f) first cycle  $dQ/dV$  versus voltage curve, and g) cycling stability of HPEIC-NMC811|Li SSB at 0.5 and 1 C.

retention of 64.42% and 60.00%, respectively. The direct wrapping of HPE on the surface of cathode particles, including high voltage cathode (NMC811), provided excellent solid–solid interface contact, which improved battery performance at 25 °C. Figure 9f shows the differential capacity ( $dQ/dV$ ) versus potential curves of the HPEIC-NMC811|Li SSB. It exhibits oxidation peaks at 3.62, 3.75, 4.01, and 4.19 V during charge, which are attributed to the multi-phase transition.<sup>[41]</sup> The phase transitions are associated with hexagonal to monoclinic, monoclinic to hexagonal, and hexagonal to hexagonal, comparable to the phase shifts determined in LIBs with liquid electrolyte.<sup>[46,47]</sup> As

a result, the HPEIC design does not alter the redox process of the cathode materials and exhibits comparable electrochemical performance to conventional LIBs with liquid electrolytes. The CV was performed to explore the electrochemical stability of SPE, HPEs, and HPEIC with LFP cathode at different scan rates (0.1, 0.5, and 1 mV s<sup>-1</sup>) as shown in Figure S8, Supporting Information. All the SSBs show a well-resolved oxidation and reduction peak around 3.6 and 3.22 V at 0.1 mV s<sup>-1</sup>, which correspond to the Fe<sup>2+</sup> to Fe<sup>3+</sup> and Fe<sup>3+</sup> to Fe<sup>2+</sup> redox reactions of LFP cathodes and are comparable to liquid electrolyte-based LFP LIBs.<sup>[41]</sup> The LFP|SPE|Li cell exhibits redox peaks at

3.822 and 3.02 V at  $0.1 \text{ mV s}^{-1}$ , with a significant potential difference between the oxidation and reduction peaks (802 mV), implying poor reversibility and cycle stability due to low ionic conductivity and transference number of the SPE. No excessive oxidation and reduction peaks are detected in the CV curves of LFP|SPE|Li, LFP|HPE-AL-LLZO:15|Li, LFP|HPE-AL-LLZO:25|Li, and HPEIC/Li SSBs, showing superior electrochemical stability.

## 2.6. Post-Mortem Analysis of Solid-State Cells

The post-mortem analysis of solid-state cells is crucial in demonstrating the mechanism of improved electrochemical performance of core-shell structure-based HPEIC and the role of Al-LLZO ceramic nanofibers in dendrite suppression

and cycling stability. **Figure 10a–g** shows post-FE-SEM micrographs of the anode and cathode sides of the free-standing SPE and HPEs, as well as the anode side of the HPEIC. The SPE is severely damaged on the anode side by the aggregation of dead lithium and dendrite growth (Figure 10a). These dendritic lithium particles penetrated the SPE membrane and made contact with the cathode, resulting in a short circuit after the 121st cycle (Figure 10a,b,i), which is consistent with the symmetric cell dendrite study (Figure 6a). As a result, the cathode particles adhere to the SPE, limiting electrochemical performance. The low transference number of SPE generates non-uniform Li-deposition on the anode metal side, resulting in aggregated dead lithium, dendrites, and particle aggregation. The mechanical strength of SPE is insufficient to suppress dendritic nucleation growth during the charge and discharge

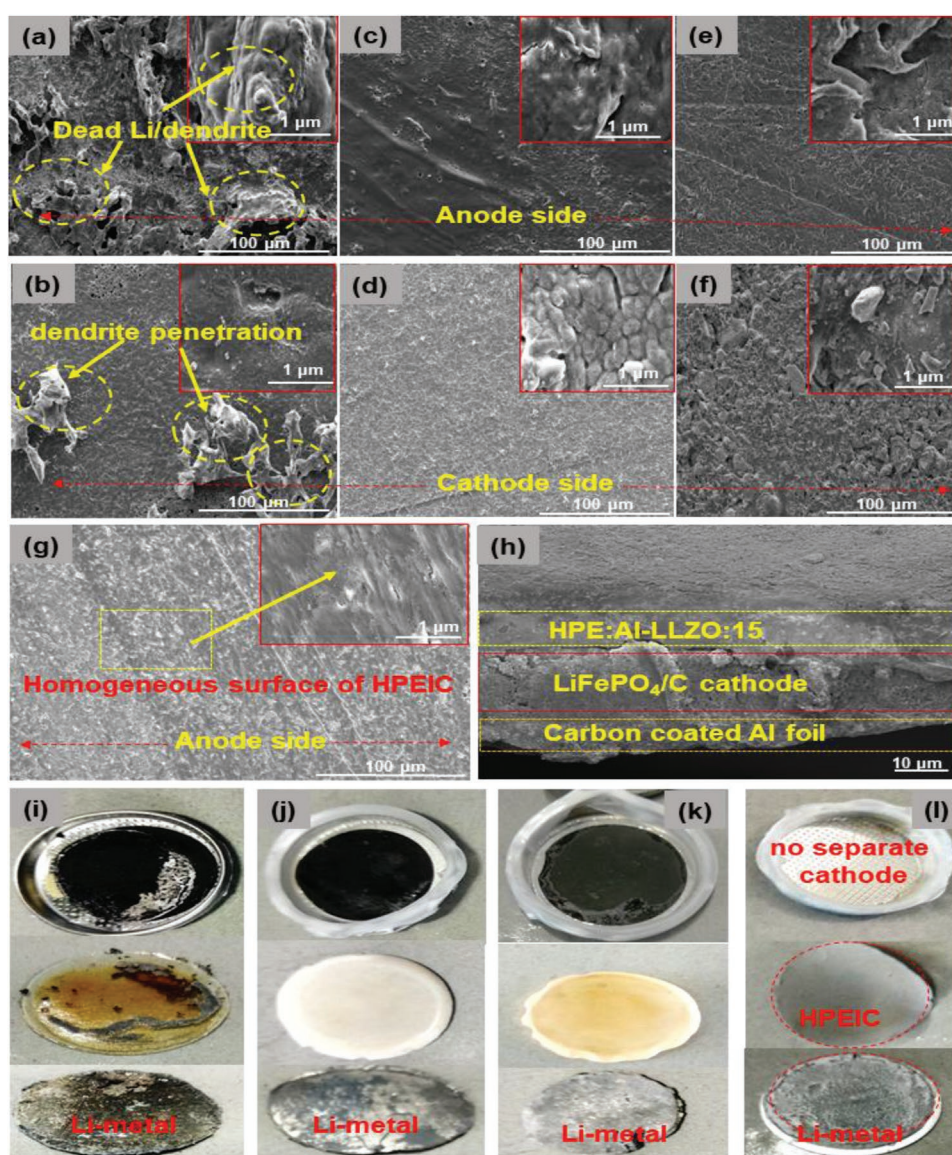


**Figure 10.** Post FE-SEM micrographs after cycling. a,c,e,g) Facing anode side and b,d,f) facing cathode side. a,b) SPE, c,d) HPE with 15 wt% Al-LLZO, e,f) HPE with 25 wt% Al-LLZO; g) Surface and h) cross-sectional FE-SEM of HPEIC. Photographs of disassembled SSBs; i) LFP/SPE/Li, j) LFP/HPE:Al-LLZO:15/Li, k) LFP/HPE:Al-LLZO:25/Li SSBs, and l) HPEIC/Li SSB.

process, which increases internal resistance and causes significant capacity fading. These issues are significantly reduced by incorporating Al-LLZO ceramic nanofibers into SPE. There are no dendrite-based aggregated particles on either the anode or cathode side of the HPE membranes shown in Figure 10c–f, and the cathode particles are not directly adherent to the HPE membranes (Figure 10j,k). The high transference number and good ionic conductivity of HPE membranes facilitate uniform Li-deposition, preventing aggregated dead Li-particles from forming at the interface between electrode and electrolyte. In addition, its high mechanical strength can suppress dendritic growth and penetration, as evidenced by the GCD profile of symmetric cells (Figure 6a,e). However, the poor interface contact between the free-standing electrolyte and electrodes affects the surface morphology of the HPE membranes. It increases internal resistance, significantly reducing the capacity, rate performance, and cycling stability of conventional SSBs. The interesting results are obtained from the interface-based core–shell structure HPEIC, as shown in Figure 10g,h,l. After 300 charge–discharge cycles, the anode side of HPEIC shows a homogeneous morphology without any agglomerated dead Li or cathode particles, implying the excellent interface contact between HPE and cathode (Figure 10g). The integrated HPEIC/Li SSB offered excellent capacity, rate capability, and cycling stability.

Furthermore, even after 300 cycles, the interface-based core–shell design is not fractured and still maintains a uniform interface between electrode/electrolyte (Figure 10h), indicating that this is a viable strategy to improve interface-based concerns in all-SSB research and scalable manufacturing. The current work's next goal is to explore and optimize the thickness, electrode size, and anode type on the design of an interface-based core–shell structure on the electrochemical performance of HPEIC, as well as to develop a prototype SSB for practical applications.

### 3. Conclusion

Al-LLZO ceramic nanofibers were synthesized by optimizing electrospinning processes and employed to prepare a hybrid PVDF/LiTFSI/Al-LLZO solid polymer electrolyte for room temperature SSBs. The influence of Al-LLZO ceramic nanofibers on the structural, morphological, electrical, and electrochemical properties of HPE was thoroughly explored. The present work proposed a unique strategy to address the significant barrier of poor interface contact between electrode and electrolyte by designing an interface-based core–shell structure with direct integration of HPE on a porous cathode surface. This technique yields an ultrathin solid polymer electrolyte with a thickness of 7  $\mu\text{m}$  which is the thinnest solid electrolyte among the LLZO CPEs reported in the literature. The HPEIC-LFP/Li SSB at room temperature (25  $^{\circ}\text{C}$ ) delivered an excellent initial specific capacity of 166  $\text{mAh g}^{-1}$  at 0.1 C rate and 159  $\text{mAh g}^{-1}$  after 120 cycles at 0.5 C with capacity retention of 100% and coulombic efficiency of 99.79%, indicating excellent cycling stability. In addition, the HPEIC-NMC811/Li SSB delivered the discharge capacity of 134  $\text{mAh g}^{-1}$  after 120 cycles at 0.5 C rate. The rational design of interface-based core–shell structured HPEIC exhibits low internal resistance and high Li-ion diffusion; it

outperforms the conventional assembly of solid-state cells in specific capacity, internal resistance, and rate performance. The major interface-based challenges of SSBs were addressed by designing an interface-based core–shell structure HPEIC, which enables the scalable manufacture and practical application of SSBs.

### 4. Experimental Section

**Materials:** The  $\text{LiNO}_3$  (99.99% Sigma-Aldrich), zirconium (IV) propoxide (70 wt% in 1-propanol, Sigma-Aldrich),  $\text{La}(\text{NO}_3)_3 \cdot 6\text{H}_2\text{O}$  (99.90%, Sigma-Aldrich),  $\text{Al}(\text{NO}_3)_3 \cdot 9\text{H}_2\text{O}$  (99.99%, Sigma-Aldrich), PVP (average  $M_w \approx 1300000$ , Sigma-Aldrich), dimethylformamide (DMF) (99.9%, Sigma-Aldrich), bis(trifluoromethanesulfoneimide) lithium salt (LiTFSI) (99.99%, Sigma-Aldrich), glacial acetic acid (Sigma-Aldrich), PVDF based binder (99.95%, MTI) were used for the preparation of Al-doped  $\text{Li}_7\text{La}_3\text{Zr}_2\text{O}_{12}$  (Al-LLZO) ceramic nanofibers and solid polymer electrolytes.

**Fabrication of Al-LLZO Ceramic Nanofibers:** Al-LLZO ceramic nanofibers with a cubic structure was synthesized using electrospinning techniques (Scheme 1a). The Al-LLZO precursor solution was prepared by dissolving stoichiometric amounts of lithium nitrate, lanthanum (III) nitrate hexahydrate, and aluminum nitrate in 10 mL DMF solvent and stirring for 3 h at room temperature (Solution A). In 2 mL acetic acid, a stoichiometric amount of zirconium (IV) *n*-propoxide was mixed and agitated until a milky white color appeared (solution B). Solution A was poured into solution B and stirred for 6 h (solution C). The appropriate wt% PVP (optimized PVP by varying the concentration) was added to solution C with continuous stirring at room temperature overnight. The precursor solutions were electrospun to produce interconnected Al-LLZO ceramic nanofibers. The following electrospinning parameters were optimized in this study: Feeding rate 0.5  $\text{mL h}^{-1}$ , DC voltage 18 kV, the distance between drum collector and needle 17 cm, and rotation speed 300 rpm. The as-spun Al-LLZO nanofibers were separated from the nonwoven fabric and dried overnight in a vacuum oven at 100  $^{\circ}\text{C}$ . The Al-LLZO nanofibers were then calcined for 3 h at three different temperatures (600, 700, and 800  $^{\circ}\text{C}$ ) at a heating rate of 1  $^{\circ}\text{C min}^{-1}$ .

**Preparation of Hybrid Polymer Electrolytes:** The free-standing SPE (PVDF/LiTFSI) was synthesized by dispersing 75 wt% PVDF in *N*-methyl-2-pyrrolidone (NMP) for 5 h at 50  $^{\circ}\text{C}$ . The 25 wt% LiTFSI was added to the PVDF/NMP solution and stirred for 24 h at room temperature; the resultant solution was coated on a glass plate (20 cm width and 25 cm length) using an electrode coating machine through the doctor blade method. The coated solution was then vacuum dried for 12 h at 80  $^{\circ}\text{C}$  to evaporate the solvent and yield the free-standing SPE. The same procedure was used to prepare the free-standing HPEs by dispersing different compositions (wt%) of Al-LLZO ceramic nanofibers into the SPE solution and obtaining the free-standing thin HPEs with a thickness of  $\approx 35\text{--}39 \mu\text{m}$ . The sample compositions and designations are as follows: SPE (PVDF/LiTFSI:75/25 wt%), HPE:Al-LLZO:5 (PVDF/LiTFSI/Al-LLZO: 70/25/5 wt%), HPE:Al-LLZO:10 (PVDF/LiTFSI/Al-LLZO:65/25/10 wt%), HPE:Al-LLZO:15 (PVDF/LiTFSI/Al-LLZO: 60/25/15 wt%), HPE:Al-LLZO:20 (PVDF/LiTFSI/Al-LLZO: 55/25/20 wt%), and HPE:Al-LLZO:25 (PVDF/LiTFSI/Al-LLZO: 50/25/25 wt%).

**Design of Interface-Based Core–Shell Structure Integrated Cathode/Ultra-Thin Hybrid Polymer Electrolytes:** The cathode electrode was prepared by mixing commercial LFP powder (MTI Co.), PVDF binder and super P carbon (MTI Co.) as a conductive additive (weight ratio—8:1:1) into NMP. The mixer was stirred for 12 h to get a homogeneous viscose slurry. The slurry was coated on the carbon-coated aluminum foil with a doctor blade and dried for 15 h at 100  $^{\circ}\text{C}$  in a vacuum oven to remove the solvent. The same procedure was employed for the preparation of the NMC811 electrode. The mass density of the electrode ( $\text{g cm}^{-2}$ ) was balanced by calendaring the coated electrode. The average loading mass of the LFP and NMC811 cathode was 3.752 mg (2.452  $\text{mg cm}^{-2}$ ) and 4.5018 mg (2.942  $\text{mg cm}^{-2}$ ), respectively. The optimized composition



15 wt% Al-LLZO ceramic nanofibers incorporated PVDF/LiTFSI HPE was chosen to design an interface-based core-shell structure by directly integrating HPE on a cathode coated electrode (HPEIC). A low viscous gel solution (5 wt% to the solvent) of HPE with carbon additive (super P carbon for electronic conductivity) was prepared by dispersing the optimized composition of PVDF, LiTFSI, and Al-LLZO nanofibers in NMP solution and stirring for 48 h at 40 °C and 400 rpm. The low viscous HPE gel solution was dropwise (0.1 mL cm<sup>-2</sup>) coated on LFP cathode and dried overnight at 60 °C in a vacuum oven. A slightly higher viscous gel solution (10 wt% to the solvent) of HPE with carbon additive was then deposited on the low viscous HPE coated LFP cathode and dried in a vacuum oven at 60 °C. In this process, the pores and micro-voids in the cathode were filled with HPE polymer, which also wrapped the LFP particles on the cathode's surface (Scheme 1b). Then an ultrathin layer of HPE slurry was coated on the HPE integrated LFP electrode via the doctor blade method using an electrode coating machine. The integrated HPEIC was vacuum-dried overnight at 100 °C to remove solvent residues that generated the interface-based core-shell structure integrated cathode/electrolyte frameworks. The same procedure was employed to design the NMC811 cathode integrated HPEIC-NMC811 system. The integrated HPEIC was kept in a glove box with <0.1 ppm water content and <0.1 ppm oxygen content. All the SPE, HPEs, and integrated HPEIC samples were punched into appropriate sizes and dried at 80 °C in a high vacuum oven for 12–18 h before assembling the solid-state cells.

**Solid-State Battery Assembly:** The CR2032-type conventional all solid-state coin cells were fabricated by sandwiching free-standing SPE and HPEs between a Li metal disk and LFP cathode. The integrated all-solid-state coin batteries were made by directly stacking the HPEIC-LFP and HPEIC-NMC811 (cathode + electrolyte) with a lithium disk anode. The integrated HPEIC cathode/electrolyte was punched into 14 mm, and the Li-metal anode diameter was 14 mm. The HPEIC electrodes were sliced from the electrolyte side to the cathode, so that no cathode particles came outside and contacted with the anode. The SSBs were fabricated with an ideal size of HPEIC and Li disk. The edge of the HPEIC was maintained perfectly for all of the cells in the current work. All the batteries were assembled in an Ar-filled glovebox with O<sub>2</sub> and H<sub>2</sub>O levels < 0.1 ppm.

**Materials and Electrochemical Characterizations:** Thermogravimetric (TGA) analysis was performed on a TGA, TG 209 F1 libra instrument from 20 to 1100 °C and 20 to 800 °C at a heating rate of 10 °C min<sup>-1</sup> in an air and N<sub>2</sub> atmosphere. XRD measurement was performed on a Bragg-Brentano diffractometer using Cu K-α radiation (λ = 1.54187) in the 2θ range between 10° and 80°. FE-SEM examined the surface and cross-sectional morphology of the samples (FE-SEM, Zeiss Leo 1530). TEM (JEOL JEM-2200FS) and SAED was applied to investigate the crystal structure and formation of Al-LLZO ceramic nanofibers. The complexation of polymer, salt, and fillers was ensured by FTIR analysis (PerkinElmer). The mechanical performance of the solid polymer electrolytes was assessed using universal tensile testing equipment (Zwick/Roell, BT1-FR0.5TN, D14). The sample dimension for the test was 20 mm in length and 2 mm in width, and the tensile speed applied to the sample was 5 mm min<sup>-1</sup>.

EIS was used to determine the ionic conductivity of SPE and HPEs by sandwiching the membranes (12.5 mm diameter) between stainless steel electrodes in a Swagelok cell. The impedance measurement was performed in the frequency range of 8 Hz to 2 MHz with 10 mV at room temperature using an electrochemical workstation (Gamry reference 6000). The ionic conductivity of the SPEs and HPEs was estimated using the following equation:

$$\sigma = \frac{d}{A \times R_b} \quad (1)$$

where σ is total conductivity (S cm<sup>-1</sup>), d is the thickness (cm) of the solid electrolytes, A is the area (cm<sup>2</sup>) of the electrolyte, and R<sub>b</sub> is the bulk resistance (Ω) which is determined by the Nyquist plot by fitting the data using equivalent circuit model. LSV (Gamry 6000) was used to test the electrochemical stability of SPE and HPEs in the voltage range of 0 to 6 V at a scan rate of 1 mV s<sup>-1</sup>. The lithium-ion transference number (t<sub>Li+</sub>) of SPE and HPEs were calculated using the chronoamperometric

polarization method with electrochemical impedance. The following equation is used to calculate t<sub>Li+</sub>:

$$t_{Li+} = I_{ss}(\Delta V - I_o R_o) / I_o(\Delta V - I_{ss} R_s) \quad (2)$$

whereas the I<sub>ss</sub> is the steady state polarization current, ΔV is the DC voltage applied during the polarization, I<sub>o</sub> is the initial current, and R<sub>o</sub> and R<sub>s</sub> are the before and after polarization resistances of the passivating layers. The solid-state <sup>7</sup>Li NMR spectroscopy (Bruker 1 GHz AEON NMR spectrometer) was performed to examine the transportation pathways of Li-ions in the SPE and HPEs and Al-LLZO ceramic nanofibers. The symmetric Li|SPE|Li and Li|HPE(15 wt%)|Li cells were fabricated by stacking the SPE and HPE between two similar Li disks (14 mm diameter) and tested the striping/plating performance of the cells by charging/discharging in a galvanostatic mode (Arbin battery tester) at different constant current densities (0.25, 0.5, 1, 2, 4, and 7 mA cm<sup>-2</sup>) at 25 °C. For each cycle, the cells were charged for 30 min and discharged for 30 min for 1050 h. EIS was used to determine the charge transfer resistance and Li-ion diffusion in SSBs at a frequency range of 10 mHz to 100 kHz. The room temperature battery performance of conventional SSBs and integrated SSBs was examined using an Arbin battery tester and GCD at current rates of 0.1 and 0.5 C throughout a voltage range of 2.5 to 4.2 V (LFP SSBs) and 2.8–4.3 V (NMC811 SSBs) at 25 °C. The electrochemical redox process was investigated using cyclic voltammetry (CV, Gamry reference 6000) at three different scan rates of 0.1, 0.5, and 1 mV s<sup>-1</sup>.

## Supporting Information

Supporting Information is available from the Wiley Online Library or from the author.

## Acknowledgements

S.P. thanks the Bavarian Centre for Battery Technology (BayBatt), University of Bayreuth, Bayreuth, Germany, for providing the necessary financial support through the Postdoctoral Research Fellowship to carry out the work.

Open access funding enabled and organized by Projekt DEAL.

## Conflict of Interest

The authors declare no conflict of interest.

## Data Availability Statement

The data that support the findings of this study are available in the supplementary material of this article.

## Keywords

ceramic nanofibers, core-shell structures, interfaces, solid electrolytes, solid-state batteries

Received: August 31, 2022  
Revised: September 21, 2022  
Published online: November 29, 2022

- [1] K. Liu, M. Wu, H. Jiang, Y. Lin, T. Zhao, *J. Mater. Chem.* **2020**, *8*, 18802.
- [2] X. Zheng, T. Yang, J. Wei, C. Wang, M. Chen, *J. Power Sources* **2021**, *496*, 229843.

- [3] P. Sivaraj, K. P. Abhilash, P. C. Selvin, *ChemistrySelect* **2021**, 6, 12036.
- [4] F. Liang, Y. Sun, Y. Yuan, J. Huang, M. Hou, J. Lu, *Mater. Today* **2021**, 50, 418.
- [5] W. Lu, M. Xue, C. Zhang, *Energy Storage Mater.* **2021**, 39, 108.
- [6] X. Zhu, K. Wang, Y. Xu, G. Zhang, S. Li, C. Li, X. Zhang, X. Sun, X. Ge, Y. Ma, *Energy Storage Mater.* **2021**, 36, 291.
- [7] R. Fan, C. Liu, K. He, S. H.-S. Cheng, D. Chen, C. Liao, R. K. Y. Li, J. Tang, Z. Lu, *ACS Appl. Mater. Interfaces* **2020**, 12, 7222.
- [8] Y. Seo, Y. Jung, M. Park, D. Kim, *J. Membr. Sci.* **2020**, 603, 117995.
- [9] M. Wu, D. Liu, D. Qu, Z. Xie, J. Li, J. Lei, H. Tang, *ACS Appl. Mater. Interfaces* **2020**, 12, 52652.
- [10] X. Zhang, T. Liu, S. Zhang, X. Huang, B. Xu, Y. Lin, B. Xu, L. Li, C. W. Nan, Y. Shen, *J. Am. Chem. Soc.* **2017**, 139, 13779.
- [11] Z. Wan, D. Lei, W. Yang, C. Liu, K. Shi, X. Hao, L. Shen, W. Lv, B. Li, Q. H. Yang, F. Kang, Y. B. He, *Adv. Funct. Mater.* **2019**, 29.
- [12] H. Zhang, X. An, Z. Lu, L. Liu, H. Cao, Q. Xu, H. Liu, Y. Ni, *J. Power Sources* **2020**, 477, 228752.
- [13] D. K. Maurya, V. Murugadoss, S. Angaiah, *J. Phys. Chem. C* **2019**, 123, 30145.
- [14] Y. Li, W. Zhang, Q. Dou, K. W. Wong, K. M. Ng, *J. Mater. Chem.* **2019**, 7, 3391.
- [15] Y. Lu, X. Zhang, C. Xue, C. Xin, M. Li, C. wen Nan, Y. Shen, *Mater. Today Energy* **2020**, 18, 100522.
- [16] T. H. Mengesha, S. L. Beshahwured, S.-H. Wu, Y.-S. Wu, R. Jose, S. J. Lue, C.-C. Yang, *ACS Appl. Energy Mater.* **2021**, 4, 14554.
- [17] M. Zhang, P. Pan, Z. Cheng, J. Mao, L. Jiang, C. Ni, S. Park, K. Deng, Y. Hu, K. K. Fu, *Nano Lett.* **2021**, 21, 7070.
- [18] J. Nunes-Pereira, C. M. Costa, S. Lancers-Méndez, *J. Power Sources* **2015**, 281, 378.
- [19] W. Liu, N. Liu, J. Sun, P.-C. Hsu, Y. Li, H.-W. Lee, Y. Cui, *Nano Lett.* **2015**, 15, 2740.
- [20] L. Z. Fan, H. He, C. W. Nan, *Nat. Rev. Mater.* **2021**, 6, 1003.
- [21] J. Wang, Y. He, Q. Wu, Y. Zhang, Z. Li, Z. Liu, S. Huo, J. Dong, D. Zeng, H. Cheng, *Sci. Rep.* **2019**, 9, 19320.
- [22] K. Fu, Y. Gong, J. Dai, A. Gong, X. Han, Y. Yao, C. Wang, Y. Wang, Y. Chen, C. Yan, Y. Li, E. D. Wachsman, L. Hu, *Proc. Natl. Acad. Sci. U. S. A.* **2016**, 113, 7094.
- [23] Y. Meesala, Y.-K. Liao, A. Jena, N.-H. Yang, W. K. Pang, S.-F. Hu, H. Chang, C.-E. Liu, S.-C. Liao, J.-M. Chen, X. Guo, R.-S. Liu, *J. Mater. Chem.* **2019**, 7, 8589.
- [24] Y.-T. Chen, A. Jena, W. K. Pang, V. K. Peterson, H.-S. Sheu, H. Chang, R.-S. Liu, *J. Phys. Chem. C* **2017**, 121, 15565.
- [25] W. Hui, W. Pan, D. Lin, H. Li, *J. Adv. Ceram.* **2012**, 1, 2.
- [26] L. Yao, W. Cao, J. Zhao, Q. Zheng, Y. Wang, S. Jiang, Q. Pan, J. Song, Y. Zhu, M. Cao, *J. Mater. Sci. Technol.* **2022**, 127, 48.
- [27] C. Chen, H. Li, J. Jin, X. Chen, Y. Cheng, Y. Zheng, D. Liu, L. Xu, H. Song, Q. Dai, *Adv. Energy Mater.* **2017**, 7, 1700758.
- [28] P. Sivaraj, K. P. Abhilash, B. Nalini, P. Perumal, P. C. Selvin, *J. Solid State Electrochem.* **2021**, 25, 905.
- [29] P. Martins, A. C. Lopes, S. Lancers-Mendez, *Prog. Polym. Sci.* **2014**, 39, 683.
- [30] P. Sivaraj, K. P. Abhilash, B. Nalini, P. Perumal, K. Somasundaram, P. C. Selvin, *Macromol. Res.* **2020**, 28, 739.
- [31] B. Li, Q. Su, L. Yu, D. Wang, S. Ding, M. Zhang, G. Du, B. Xu, *ACS Appl. Mater. Interfaces* **2019**, 11, 42206.
- [32] L. Liu, J. Lyu, J. Mo, H. Yan, L. Xu, P. Peng, J. Li, B. Jiang, L. Chu, M. Li, *Nano Energy* **2020**, 69, 104398.
- [33] Y. Lin, M. Wu, J. Sun, L. Zhang, Q. Jian, T. Zhao, *Adv. Energy Mater.* **2021**, 11, 2101612.
- [34] P. Sivaraj, K. P. Abhilash, B. Nalini, P. C. Selvin, S. Goel, S. K. Yadav, *J. Am. Ceram. Soc.* **2020**, 103, 1685.
- [35] T. Yang, J. Zheng, Q. Cheng, Y. Y. Hu, C. K. Chan, *ACS Appl. Mater. Interfaces* **2017**, 9, 21773.
- [36] F. Lu, X. Gao, A. Wu, N. Sun, L. Shi, L. Zheng, *J. Phys. Chem.* **2017**, 121, 17756.
- [37] C. Fritsch, T. Zinkevich, S. Indris, M. Etter, V. Baran, T. Bergfeldt, M. Knapp, H. Ehrenberg, A. L. Hansen, *RSC Adv.* **2021**, 11, 30283.
- [38] M. J. Lee, J. Han, K. Lee, Y. J. Lee, B. G. Kim, K. Jung, B. J. Kim, S. W. Lee, *Nature* **2022**, 601, 217.
- [39] Z. Guo, Y. Pang, S. Xia, F. Xu, J. Yang, L. Sun, S. Zheng, *Adv. Sci.* **2021**, 8, 2100899.
- [40] H. Erabhoina, M. Thelakkat, *Sci. Rep.* **2022**, 12, 5454.
- [41] X. Liu, Y. Zhang, Y. Meng, T. Kang, H. Gao, L. Huang, F. Zhu, *ACS Appl. Energy Mater.* **2022**, 7, 8452.
- [42] C. Han, W. Q. Cao, M. S. Caonorg, *Chem. Front.* **2020**, 7, 4101.
- [43] L. H. Yao, W. Q. Cao, J. C. Shu, M. S. Cao, X. D. Sun, *Chem. Eng. J.* **2021**, 413, 127428.
- [44] W. Cao, W. Wang, H. Shi, J. Wang, M. Cao, Y. Liang, M. Zhu, *Nano Res.* **2018**, 11, 1437.
- [45] F. Xin, H. Zhou, Y. Zong, M. Zuba, Y. Chen, N. A. Chernova, J. Bai, B. Pei, A. Goel, J. Rana, F. Wang, *ACS Energy Lett.* **2021**, 6, 1377.
- [46] K. Marker, P. J. Reeves, C. Xu, K. J. Griffith, C. P. Grey, *Chem. Mater.* **2019**, 31, 2545.
- [47] S. Shrestha, J. Kim, J. Jeong, H. J. Lee, S. C. Kim, H. J. Hah, K. Oh, S. H. Lee, *J. Electrochem. Soc.* **2021**, 168, 060537.